Tuning the hydride stability of the TiVNb-based alloys by equimolar Cr/Al addition

Tales Ferreira, Nayely Pineda-Romero, Walter José Botta, Guilherme Zepon, Claudia Zlotea

Tuning the hydride stability of the TiVNb-based alloys by equimolar Cr/Al addition

Tales Ferreira[a,b]*, Nayely Pineda-Romero[a], Walter José Botta[b], Guilherme Zepon[b], Claudia Zlotea[a]

[a] Univ. Paris Est Creteil, CNRS, ICMPE, UMR 7182, 2 Rue Henri Dunant, 94320 Thiais, France

[b] Departamento de Engenharia de Materiais, Universidade Federal de São Carlos, São Carlos, Rod. Washington Luiz, km 235, São Carlos, SP 13565-905, Brazil

* Corresponding author. Postal address: University Paris Est Créteil, CNRS, ICMPE, UMR 7182, 2 Rue Henri Dunant, 94320 Thiais, France.

E-mail adresses: tferreira.tales@gmail.com (T. Ferreira).

ABSTRACT

Body-centered multi-principal element alloys (BCC-MPEAs) based only on hydride-forming elements have low equilibrium plateau pressures during reaction with hydrogen and, consequently, high decomposition temperatures due to the high thermodynamic stability of related hydrides. In this work, we present a strategy to decrease the stability of the final hydrides formed in the BCC TiVNb alloy by simultaneous addition of two non-hydride forming elements, Cr and Al. The $(TiVNb)_{100-x}(CrAl)_x$ alloys with x = 10, 20, 30, and 40 at.% crystallize as major BCC solid solutions with dendritic microstructures. Pressure-Composition-Temperature diagrams revealed that the combined addition of Cr and Al thermodynamically destabilizes the dihydride formation for x = 10 and 20 at.%. For higher Cr/Al contents the destabilization is too large to form stable hydrides under maximum 100 bar pressure. The absorption/desorption plateau pressure at room temperature for $(TiVNb)_{80}(CrAl)_{20}$ alloy are 9 and 0.6 bar, respectively, enabling a reversible capacity of about 0.8 H/M (1.4 wt.%) at ambient conditions. The present results provide important insights into the effects of simultaneous Cr and Al additions in BCC-MPEAs and shed light on the design of new alloys with hydrogen absorption and desorption ability at ambient conditions.

Keywords: Multi-principal element alloys; Hydrogen storage; Metal hydrides; Thermodynamic; Thermo-desorption spectroscopy; absorption/desorption cycling.

1. Introduction

Hydrogen economy holds a promising prospect to change the current energy economy based on fossil fuel to an energy carriers based on renewable and clean sources [1]. In this context, hydrogen produced by water electrolysis or biomass reform, namely, the green hydrogen, represents the most promising energy carrier for the development of the low-carbon economy. However, several scientific and technological challenges still need to be overcame to implement hydrogen as an energy carrier on a large scale. One of the key issues for the widespread use of hydrogen-based energy is its safe, compact, and efficient storage and transportation [2]. Among the different types of materials that have been studied for this application [3], metal hydrides (MHs) have been considered as one of the most promising for solid-state-based hydrogen storage, providing safety and high volumetric densities [4].

Multi-principal element alloys (MPEAs), a recent and very promising alloying strategy, are currently under the intense focus of the scientific community due to their interesting properties. These new alloys are based on the exploration of systems having three or more main elements with equiatomic or near equiatomic fractions, which can lead to the formation of simple single-phase solid solutions, i.e., body-centered cubic (BCC, Im-3m) solid solutions [5,6]. The research is focused to the center area of multicomponent phase diagrams which is still largely unexplored. This can lead to the discovery of new materials with exceptional properties. Among MPEAs, alloys with at least five principal elements with atomic concentrations between 5 and 35% are called high entropy alloys (HEAs).

The first refractory BCC-MPEA with promising hydrogen storage properties was reported in 2016 [7]. During hydrogen absorption, the TiVZrNbHf alloy formed a body-centered tetragonal (BCT, I4/mmm) hydride with high hydrogen storage capacity (2.7 wt%). Since then, several BCC-MPEAs, commonly composed of refractory elements with high hydrogen affinity (such as Ti, V, Nb, Zr, Hf, Ta), have been reported with interesting properties which makes

them a very promising class of materials for solid-state hydrogen storage [8–10]. Nevertheless, one of the main drawbacks of BCC-MPEAs based only on refractory elements is the high thermodynamic stability of its hydride, which prevents the desorption process to occur under moderate temperature and pressure conditions. The equimolar TiVNb alloy is a typical and important example of such case. Nygard et al. [11] reported that this BCC solid solution in the as-cast state rapidly absorb hydrogen forming an FCC hydride (CaF_2-type structure) with the maximum capacity of about 2 H/M (3.2 wt.%). Despite a high capacity and fast kinetic of absorption at room-temperature, the TiVNb alloy has a very low equilibrium plateau pressure and very high onset temperature for hydrogen desorption (T_{onset}). As these properties are highly dependent on their chemical composition, the addition of non-hydride forming elements has been reported as a potential solution to overcome these drawbacks of refractory BCC-MPEAs and to tune their hydrogen storage properties [11,12]. In this context, two additional elements are identified as promising candidates, chromium and aluminum, as described below.

Nygard et al. [11] synthesized by arc-melting the equiatomic TiVNbCr alloy and showed that the T_{onset} was reduced by the addition of Cr into the ternary alloy. Strozi et al. [13] showed that, without significant loss of maximum capacity, the equilibrium pressure of $(TiVNb)_{100-x}Cr_x$ alloys (with x = 15, 25 and 35 at.%) at room temperature increases as the Cr content raises. Recently, the same authors investigated the thermodynamic properties of these alloys with x = 30, 35 and 40 at.% [14]. These results showed a shift of the absorption/desorption plateau pressures from 0.3 bar / 0.1 bar to 1.8 bar / 0.4 bar at 30 °C with increasing Cr content from 30 to 35 at.%. Consequently, the enthalpy for hydrogen absorption and desorption decreased with the increase of the Cr content. Furthermore, both alloys showed a reversible hydrogen absorption/desorption of about 1 H/M at 30 °C. However, a further increase in the equilibrium plateau pressure by increasing Cr content above 35 % was not possible. It was demonstrated that increasing Cr content to 40 at.% leads to the formation of a major C15 phase at the expense

of the BCC solid solution, which has small hydrogen storage capacity. The main motivation of the present study is to search a second element to be concomitantly added with Cr that could stabilize the BCC solid solution and lead to a fine tuning of the thermodynamic properties of the ternary TiVNb alloy during reaction with hydrogen.

In this context, aluminum is a strategic and promising element for hydrogen storage materials because it is lightweight, inexpensive, and earth-abundant [15]. To explore the potential of this element to reduce the density of alloys, the influence of Al content on the phase formation and mechanical properties of BCC-MPEAs has been investigated in different systems, i.e., AlNbTaTiZr-(Mo or Hf) [16], AlNbTiMoV [17], and AlNbTiV [18]. However, studies reporting the effect of this element on the hydrogen storage properties of BCC-MPEAs are scarce in the literature. Two studies on the effect of 10 at.% Al addition into the BCC lattices of TiVNbZr [19] and TiVNb [20] alloys have been recently reported. After exposure to hydrogen gas, the BCC $Al_{0.10}Ti_{0.30}V_{0.25}Zr_{0.10}Nb_{0.25}$ alloy transformed into a BCT hydride with a storage capacity of 1.6 H/M (2.6 wt.%) [19]. On the other hand, the BCC $Al_{0.10}Ti_{0.30}V_{0.30}Nb_{0.30}$ solid solution formed an FCC hydride with a similar hydrogen uptake of 1.59 H/M (2.6 wt.%) [20]. For both BCC alloys, the main improvements due to the addition of 10 at.% Al were a reduction of the T_{onset} desorption temperature and an improvement in the cycling stability without significant loss of capacity. Recently, Pineda-Romero et al. [21] investigated the hydrogen storage properties of the ternary TiVNb alloy from low Al content up to equimolar composition and showed that Al influences hydrogen thermodynamics more effectively than Cr. The authors demonstrated that the enthalpy of FCC hydride in the TiVNb alloy decreases from -67 kJ/mol H_2 to -49 kJ/mol H_2 after adding 10 at.% of Al.[20,21].

Based on the literature above, we hypothesized that adding both Cr and Al into the TiVNb alloy could maintain the BCC solid solution of the initial alloys while decreasing the stability of the hydrides, enabling a better tuning of the equilibrium plateau pressure. Therefore, with

this goal in mind, the $(TiVNb)_{100-x}(CrAl)_x$ alloys with x = 10, 20, 30, 40 at.% were experimentally produced by arc melting and their physicochemical and hydrogen storage properties investigated.

2. Experimental procedure

The equilibrium phases of $(TiVNb)_{100-x}(CrAl)_x$ alloys with x = 10, 20, 30, and 40 at.% were investigated trough thermodynamic calculation using CALPHAD method. Thermo-Calc® [22] software and TCHEA5 database were employed. The four chemical compositions were synthetized by arc melting under an inert argon atmosphere. High purity metals from pieces of Ti (Alfa Aesar, 99.99%), V (NEYCO Vacuum&Materials, 99.9%), Nb (Alfa Aesar, 99.95%), Cr (Chempur, 99.99%) and Al (STREM Chem, 99%) were used as feedstock material. The alloys were produced by melting initially only Ti, V, Nb and Cr pieces to form a quaternary alloy and, subsequently, Al pieces were added and melted to obtain the desired chemical composition. This procedure was adopted due the low melting temperature of Al relative to the rest of components and to avoid loss of this element. The alloys, before and after Al addition, were remelted five times and flipped between each melting step to improve the homogeneous distribution of the elements.

The microstructural investigations were carried out using a scanning electron microscope (SEM) Zeiss Merlin instrument, equipped with energy-dispersive X-ray spectroscopy (EDX) detector from Oxford Instruments. Prior to SEM and EDX analysis, samples were embedded into resin, grinded and polished using standard metallography procedures. The phase identification was performed by X-ray diffraction (XRD) in a D8 Advance Bruker diffractometer using Cu-Kα radiation. The lattice parameters of the present phases were determined by Rietveld refinement method using the software General Structure Analysis System II (GSAS-II) [23].

For examination of hydrogen storage performance, approximately 300 mg of small pieces of alloys were loaded into a stainless-steel sample holder of a home-made Sieverts-apparatus. Prior to volumetric measurements, the samples were heat treated at 400 °C for 12h under a dynamic primary vacuum and subsequently cooled to room-temperature (RT). This common practice procedure for metal hydrides, called activation [24], is generally carried out to avoid any deleterious effect of oxide layers at surface during the first absorption. After activation, kinetics measurements were performed at 25 °C exposing each sample to a final equilibrium pressure of 75 bar of hydrogen. The isothermal (25 °C) condition was ensured by placing the sample holder in a temperature-controlled water bath. The determination of Pressure-Composition-Temperature (PCT) diagrams were conducted at different temperatures so that the thermodynamic of hydrogen absorption/desorption could be evaluated. For the acquisition of the PCT curves at high (>RT) or low (<RT) temperatures, a resistive furnace or an industrial water cooler equipment were employed, respectively.

Thermal desorption spectroscopy (TDS) measurements were performed by a home-made instrument coupled to a quadrupole mass spectrometer (QMS) to keep track the partial pressures of released gases during a constant heating ramp of 5 °C/min. Approximately 10 mg of the hydrogenated sample were loaded into an aluminum crucible and then the measurement was performed under dynamic secondary vacuum pump.

3. Results and discussion

3.1. Thermodynamic calculations

Targeting a clearer understanding of phase formation and the effects of both Cr and Al additions into the $(TiVNb)_{100-x}(CrAl)_x$ alloys, the equilibrium solidification paths for these alloys were calculated and shown in Fig. 1 with x = 10 (Fig. 1a), 20 (Fig. 1b), 30 (Fig. 1c), and

40 at.% (Fig. 1d). For all the alloys, the solidification starts with the formation of the BCC solid solution. For the alloy with the lower Cr and Al addition (Fig. 1a and x = 10 at.%), the thermodynamic calculation suggests that, under equilibrium conditions, the orthorhombic O_Phase (Cmcm space group) could precipitate. This O_Phase has been reported as the main strengthening phase in Ti_2AlNb-based alloys [25]. For x = 20 at.% (Fig. 1b), the stability field of the O_Phase increases at the expense of the BCC region, which is still large. Furthermore, the precipitation of a second BCC is also predicted. Further Cr and Al addition leads to precipitation of multi-secondary phases. Among them, the C14_Laves phase has the highest precipitation temperature, which increases from about 1000 °C for x = 30 at.% to about 1400 °C for x = 40 at.%, Figs 1c and 1d, respectively. It should be highlighted that although the formation of secondary phases is predicted, rapid cooling rates, as employed in this work by the current melting process, have been generally considered an effective method to produce single-phase materials or disordered solid solutions with very small fractions of secondary phase precipitates. This is further validated by the structural characterization, as detailed below.

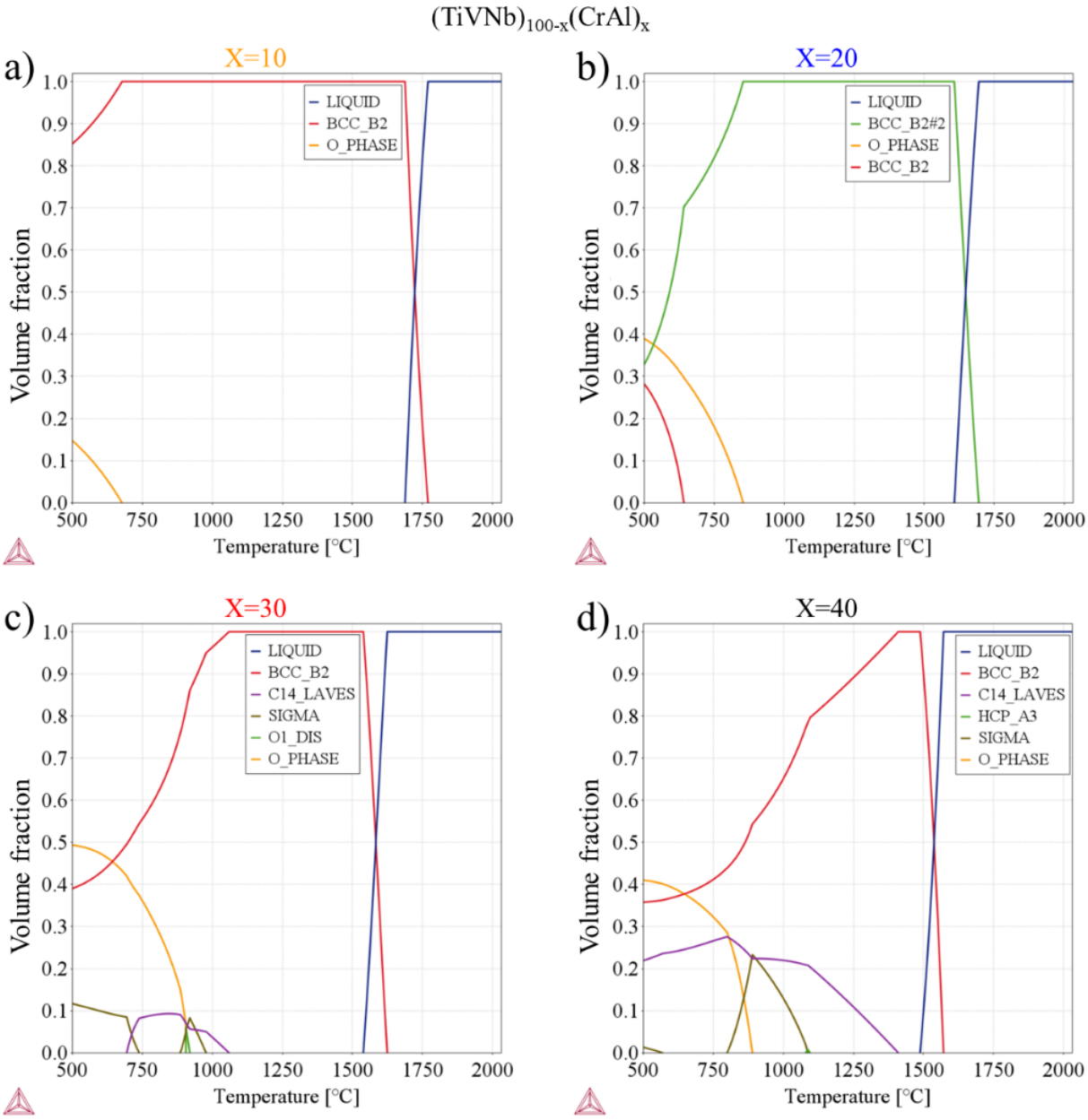

Fig. 1. Equilibrium volume fraction of phases as function of temperature for the: a) $(TiVNb)_{90}(CrAl)_{10}$, b) $(TiVNb)_{80}(CrAl)_{20}$, c) $(TiVNb)_{70}(CrAl)_{30}$ and $(TiVNb)_{60}(CrAl)_{40}$ multi-principal element alloys.

3.2. Structural characterization

Fig. 2 shows scanning electron microcopy (SEM) backscattered electron (BSE) images of the as-cast $(TiVNb)_{100-x}(CrAl)_x$ alloys with x = 10, 20, 30, and 40 at.%, respectively. One

can see that all the alloys have dendritic microstructures with different brightness intensities between the dendritic and interdendritic areas. The experimental chemical composition of these microstructures, measured by EDX, are summarized in Table 1. The high-brightness areas (dendrites' center) tend to be enriched in Nb, while the low-brightness regions (interdendrites) are slightly richer in Ti, V and Cr. It should be noted that Al showed the higher chemical homogeneity among all the elements, see the Table 1 and the EDX-SEM chemical mapping analysis for all alloys in Figures S1-S4 from the Supplementary data.

Despite these slight chemical composition differences between the dendritic and interdendritic regions, one can see that the average compositions for all the alloys are very close to the nominal ones. These small chemical modulations can be associated with solute partitioning during the solidification process and it has been observed for most of refractory MPEAs such as, the TiVNb alloy [11], the TiVNb-Cr alloys [13,26] and TiVNb-Al compositions [20,21]. Another interesting observation from Figure 2 is related to the microstructure that evolves with the change in chemical composition. It seems that the dendrite size increases with Cr/Al substitution suggesting a coarsening of the microstructure.

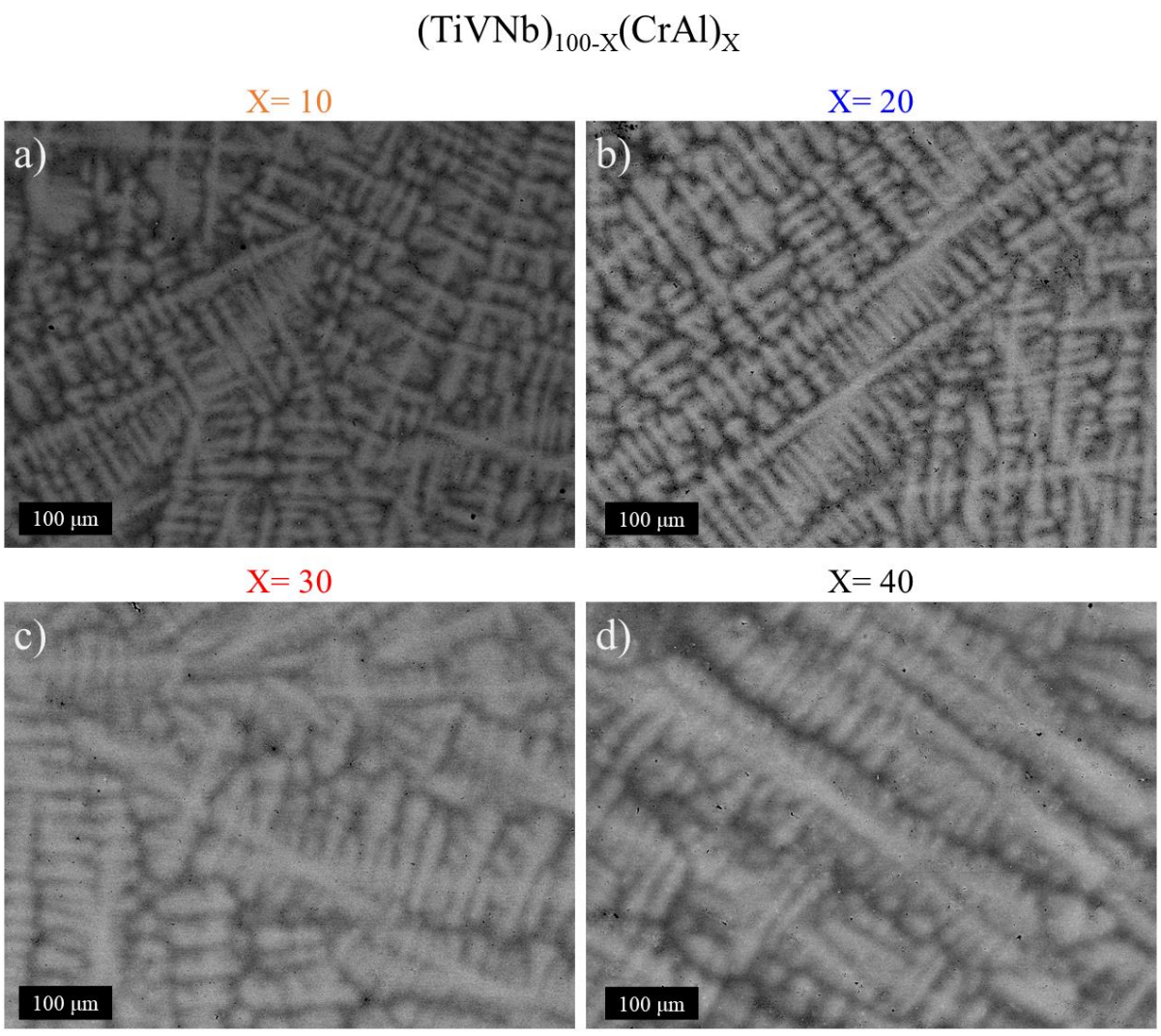

Fig. 2. SEM-BSE images of the as-cast: a) $(TiVNb)_{90}(CrAl)_{10}$, b) $(TiVNb)_{80}(CrAl)_{20}$, c) $(TiVNb)_{70}(CrAl)_{30}$, d) $(TiVNb)_{60}(CrAl)_{40}$ alloys.

The XRD patterns of the as-cast $(TiVNb)_{100-x}(CrAl)_x$ alloys series are shown in Fig. 3a. For comparison purposes, the pattern of the ternary TiVNb alloy, already published elsewhere [20], has been included. From these results, it can be confirmed that all the alloys are predominantly BCC phases. The existence of low intensity peaks in the XRD patterns of the alloys with x = 20 and 40 at.% suggests the presence of a small fraction of a secondary phase.

Figure S5 from the Supplementary Material shows the Rietveld refinements for all as-cast alloys. One can see that the equimolar Cr and Al addition into the ternary alloy reduces the BCC lattice parameter from a_{BCC}= 3.211 Å (x = 0) to a_{BCC}= 3.128 Å in the alloy with x = 40 at.%, see Fig. 3a and Figure S6 from the Supplementary data. To understand this behavior, the calculated average atomic radius and the BCC lattice parameter determined for each composition were plotted as a function of the Cr and Al content, Figure 3b. A clear and linear correlation between these two parameters can be observed, in which both were reduced as the Cr and Al contents were increased. This effect was similar when individual Cr [13] and Al [20] additions were investigated into the TiVNb alloy.

Table 1 – Chemical composition of the as-cast $(TiVNb)_{100-x}(CrAl)_x$ alloys measured by EDX (at.%). The reported values are the average of multiple measurements.

$(TiVNb)_{100-x}(CrAl)_x$	**Region**	**Ti**	**V**	**Nb**	**Cr**	**Al**
	Overall	30.7 ± 0.1	30.0 ± 0.1	29.4 ± 0.1	4.9 ± 0.1	5.0 ± 0.1
X= 10	Dendritic	29.3 ± 0.3	29.1 ± 0.5	32.5 ± 0.6	4.4 ± 0.1	4.7 ± 0.1
	Interdendritic	32.2 ± 0.4	30.9 ± 0.2	26.2 ± 0.7	5.5 ± 0.3	5.2 ± 0.2
	Overall	27.0 ± 0.2	26.3 ± 0.2	26.8 ± 0.1	9.4 ± 0.1	10.5 ± 0.1
X= 20	Dendritic	26.3 ± 0.3	25.8 ± 0.2	29.6 ± 0.7	8.2 ± 0.4	10.1 ± 0.1
	Interdendritic	28.1 ± 0.4	26.9 ± 0.2	22.5 ± 1.0	11.5 ± 0.7	11.0 ± 0.2
	Overall	23.9 ± 0.1	23.3 ± 0.1	23.5 ± 0.1	14.2 ± 0.1	15.1 ± 0.1
X= 30	Dendritic	22.9 ± 0.2	23.7 ± 0.1	26.0 ± 0.4	12.3 ± 0.3	15.1 ± 0.1
	Interdendritic	25.1 ± 0.4	22.3 ± 0.4	20.4 ± 0.9	16.7 ± 0.9	15.5 ± 0.2
	Overall	20.3 ± 0.1	19.8 ± 0.1	20.2 ± 0.1	19.6 ± 0.1	20.1 ± 0.1
X= 40	Dendritic	19.6 ± 0.2	20.8 ± 0.2	21.5 ± 0.2	17.8 ± 0.2	20.3 ± 0.1
	Interdendritic	21.1 ± 0.2	18.5 ± 0.5	18.4 ± 0.4	21.6 ± 0.6	20.4 ± 0.2

As previously mentioned, the XRD pattern of the $(TiVNb)_{60}(CrAl)_{40}$ alloy presents low intensity peaks of a secondary B2 phase (see the peak around $2\theta = 28°$ in Figure S5d). A quantitative phase analysis by Rietveld method could not be performed because of the small intensity of the diffraction peaks from the secondary phase, which confirms the low fraction of this phase. It is important to point out that the formation of the B2 phase was not predicted by thermodynamic calculations for this chemical composition. Analyzing some phase transformations from available literature data on simpler systems, it was found that B2 and O-phases can be found in Al-Nb-Ti [27] and Al-Cr-Nb-Ti [28] systems. Since the database containing the description of Al-Nb-Ti system is quite recent (2020), perhaps we can expect some deviation in the prediction of the phase stability. Low intensity peaks around $2\theta = 37°$ and 43° could also be observed in the XRD pattern of the $(TiVNb)_{80}(CrAl)_{20}$ alloy, see Figure S5b. This minor phase is associated with some Ti-rich precipitates (black phase), which could be observed in the interdendritic regions in higher magnification BSE images, see Figure S7 from the Supplementary Material. This plate-like morphology of the Ti-rich precipitates is very similar to the formation of (Ti, Al)-rich orthorhombic particles (O_Phase) reported in the TiNbHfAl [25] and TiAlNb [27] systems. The formation of O_Phase in the $(TiVNb)_{80}(CrAl)_{20}$ alloy also agrees with the thermodynamic calculations in Fig. 1b. However, EDX-SEM chemical mapping analysis, Figure S7 from the Supplementary data, clearly shows that the plate-like precipitates found in the present work are poor in Al, which is different from that previously reported for this phase [25]. Strozi et al. [13] have reported the formation of Ti-rich precipitates in TiVNb-(Cr) alloys. In a recent study, through thermodynamic calculations and experimental results, the authors demonstrated that increasing Cr content leads the formation of C15_Laves phase (Fd-3m space group) [14]. However, from the same CALPHAD approach and database (TCHEA5) used in that work, the thermodynamic calculations performed here, Fig. 1, do not suggest the formation of the C15_Laves phase in any of the the $(TiVNb)_{100-}$

$_x$(CrAl)$_x$ alloys with x = 10, 20, 30, and 40 at.%. Attempts to index the limited number of small-intensity peaks in the XRD pattern with the Cmcm and Fd-3m space groups were unsuccessful. Thus, the identification of the minor phase composed of Ti-rich plate-like precipitates demands further investigation, which is out the scope of this work.

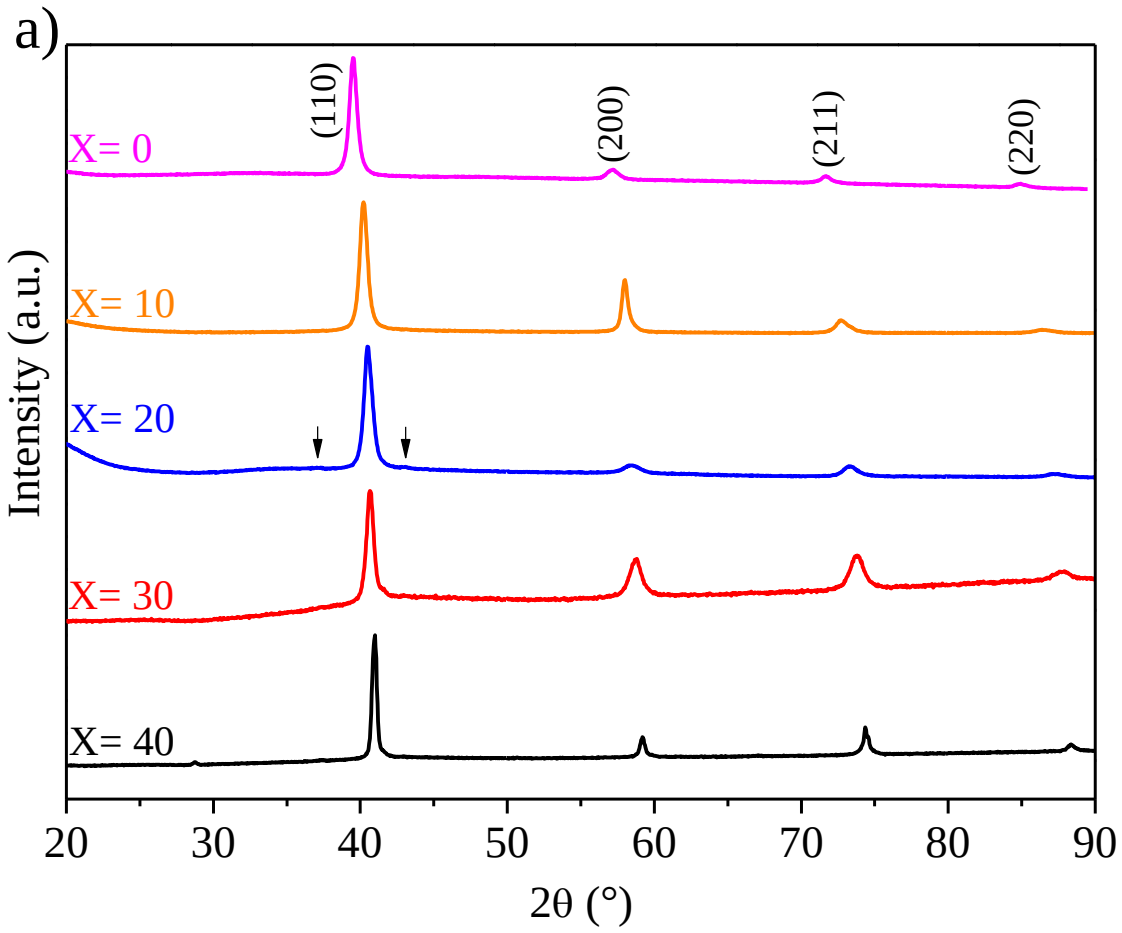

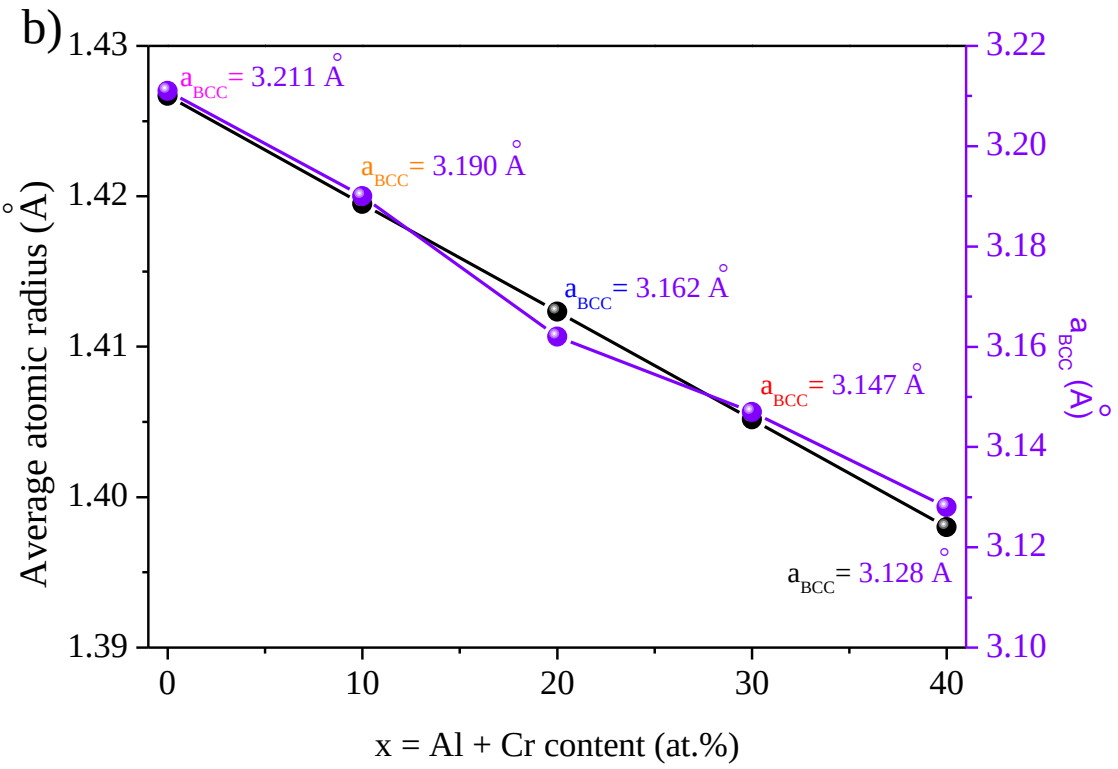

Fig. 3. (a) XRD patterns of as-cast $(TiVNb)_{100-x}(CrAl)_x$ alloys with x =0 [20], 10, 20, 30, and 40 at.%. (b) Average atomic radius and a_{BCC} lattice parameter determined for the $(TiVNb)_{100-x}(CrAl)_x$ alloys as a function of the Cr and Al content. The atomic radii considered for the Ti, V, Nb, Cr and Al elements are 1.46, 1.35, 1.47, 1.28, and 1.43 Å, respectively, as taken from reference [6]. The arrows indicate the presence of low intensity peaks in the XRD pattern of the $(TiVNb)_{80}(CrAl)_{20}$ alloy, suggesting a small fraction of secondary phases.

3.3. Hydrogen absorption kinetics at room temperature

The kinetic curves recorded at 25 °C for the $(TiVNb)_{100-x}(CrAl)_x$ alloys are plotted in Fig. 4. For the sake of comparison, the kinetic curve of the ternary TiVNb alloy, as recorded previously [20], is included. If alloys with x = 0 – 30 at.% rapidly absorb hydrogen reaching maximum capacity in less than 30 minutes, the composition with x = 40 at.% stands out with a very slow kinetics. The maximum capacity is achieved after around 250 min, suggesting that

the presence of Cr and Al are responsible for slow kinetic properties. These results will be linked and discussed further with the thermodynamic properties in the appropriate section.

The alloy with x = 10 absorbs 1.8 H/M (equivalent to 3.00 wt.%) which is smaller than 2.0 H/M for the initial TiVNb (3.2 wt.%). As identified by the XRD pattern displayed in Fig. 5a, the hydrogenation process in this alloy leads to the formation of a single-phase FCC dihydride, in agreement with the initial TiVNb alloy [20]. Interestingly, the XRD analysis for the alloy with x = 20, which achieved a capacity of 1.44 H/M (2.4 wt.%), presents a mixture of hydrogenated phases. A BCT dihydride (a = 3.067 Å, c = 4.263 Å) and a BCC hydride (a = 3.285 Å) with lattice parameter greater than the as cast BCC sample were identified. For higher Cr and Al content alloys (x = 30 and x = 40), BCC hydrides were observed with capacity of 0.66 H/M (1.2 wt.%) and 0.41 H/M (0.8 wt.%), respectively.

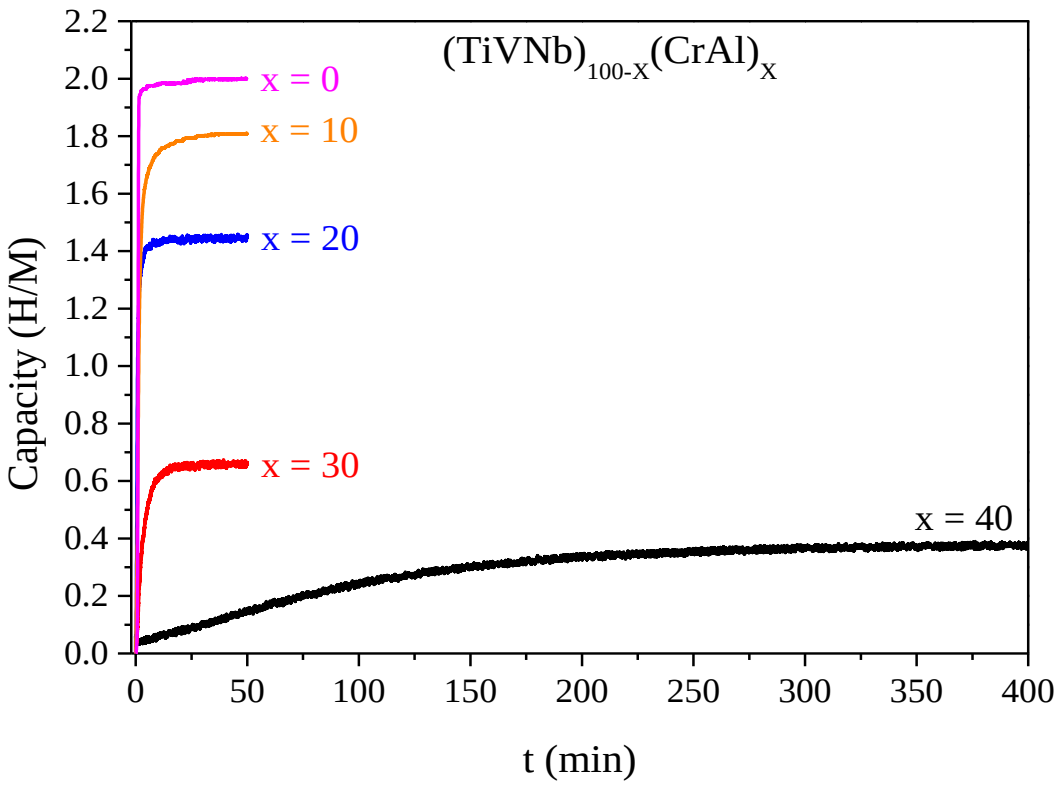

Fig. 4. Kinetic curves of the first hydrogen absorption of the $(TiVNb)_{100-x}(CrAl)_x$ alloys. Experiments were carried out at 25 °C and under a final equilibrium H_2 pressure of 75 bar. For

comparison purposes, the kinetic curve of the ternary TiVNb alloy, already published elsewhere [20], has been included.

To observe the effects of chemical composition more clearly, the maximum capacity of all alloys was plotted as a function of Cr and Al contents, see Fig. 5b. A significant decrease in the maximum capacity can be observed with the increase of Cr and Al. Although both elements added have lower hydrogen affinities compared to Ti, V and Nb (which are hydride forming elements), this effect on hydrogen storage capacity has been reported mainly for Al containing alloys. Strozi et al. [13] demonstrated that by increasing the Cr/(TiVNb) ratio in $(TiVNb)_{100-x}(Cr)_X$ alloys there is no significant loss of storage capacity up to 35 at.% whereas, Pineda-Romero et al. [21] showed that the increase of the Al/(TiVNb) ratio in $(TiVNb)_{100-x}(Al)_x$ alloys strongly reduce the storage capacity. Therefore, it seems that the reduced capacity in our alloys is mainly a consequence of Al presence and to a less extent due to Cr.

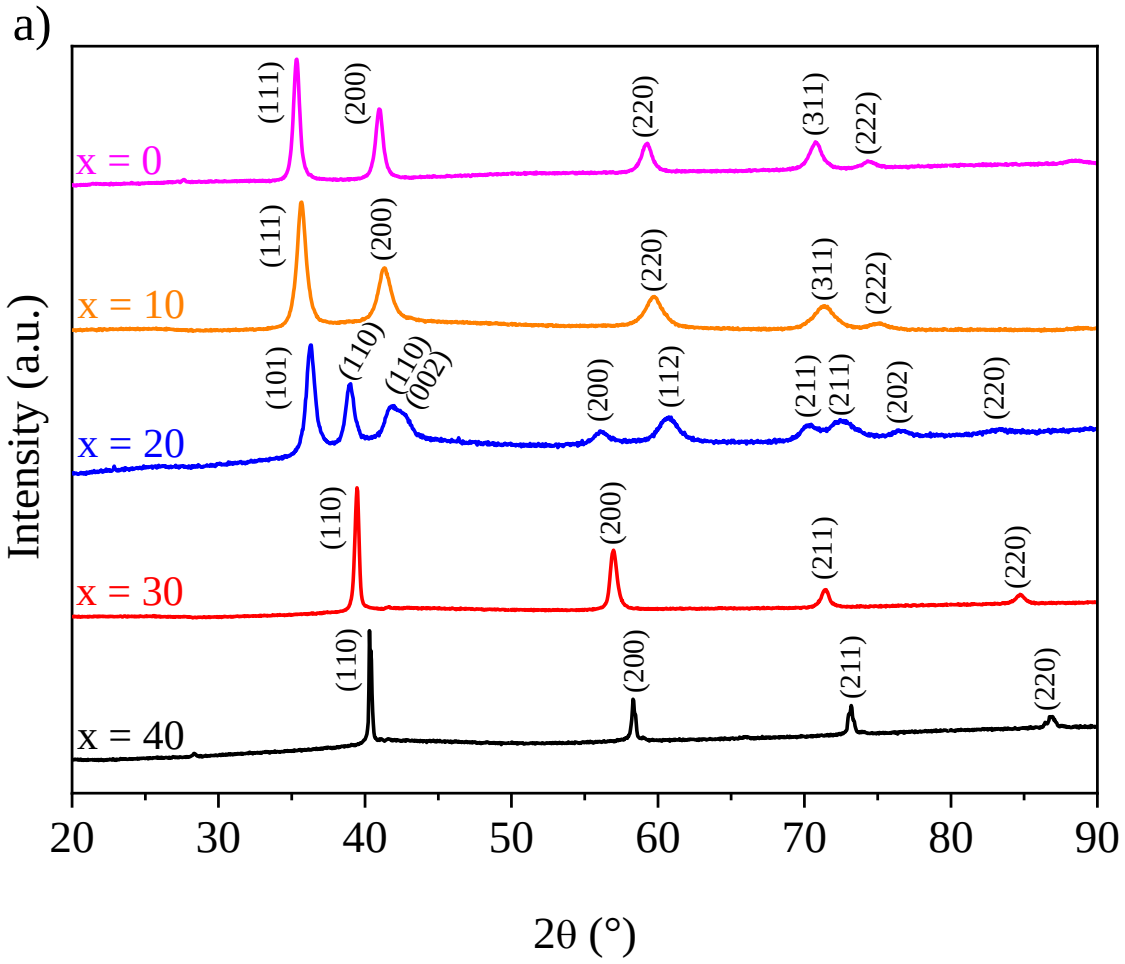
a)
x = 0
x = 10
x = 20
x = 30
x = 40
(111)
(200)
(220)
(311)
(222)
(101)
(110)
(002)
(112)
(211)
(202)
Intensity (a.u.)
2θ (°)
20
30
40
50
60
70
80
90

1

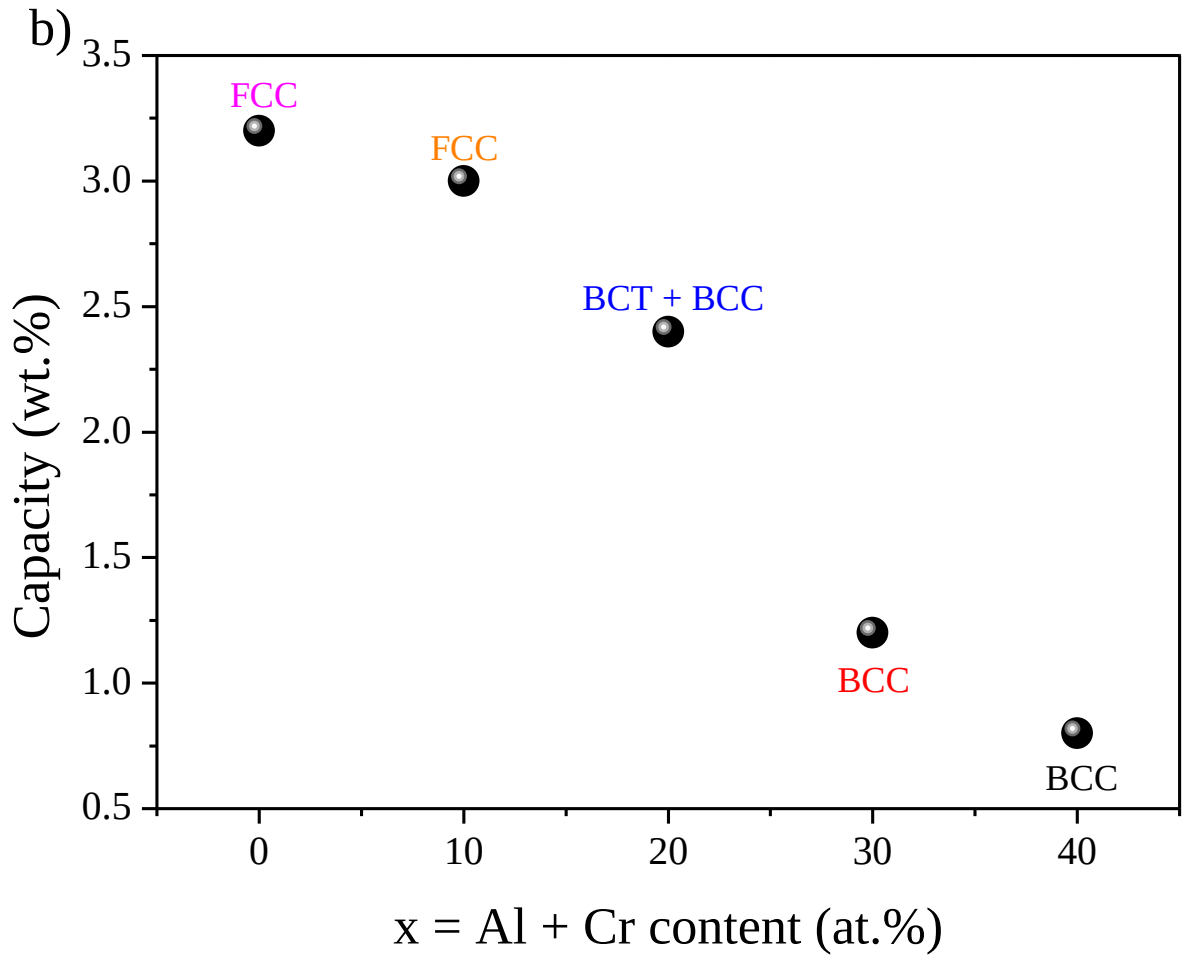

Fig. 5. (a) XRD patterns of the $(TiVNb)_{100-x}(CrAl)_x$ alloys with x = 0 [20], 10, 20, 30 and 40 at.% after the first hydrogen absorption at room temperature. (b) Hydrogen storage capacity (wt.%) of all alloys at 75 bar as a function of Cr and Al contents. The Rietveld refinements of all hydrogenated patterns are shown in Figure S8 of the supplementary data and the lattice parameters are listed in Table 2.

Table 2 – Lattice parameters of the phases formed in the $(TiVNb)_{100-x}(CrAl)_x$ alloys: as-cast, after kinetic (hydride) and after TDS (desorbed). The related Rietveld refinements can be found in Figs. S1, S8 and S10, respectively, from the Supplementary material.

Alloy	Form	Phase	Phase Fraction (%)	Lattice Parameter a/c (Å)
TiVNb	As-cast	BCC	100	3.211 (1)
	dihydride	FCC	100	4.443 (1)
	Desorbed	BCC	100	3.207 (5)
$(TiVNb)_{90}(CrAl)_{10}$	As-cast	BCC	100	3.190 (1)
	dihydride	FCC	100	4.399 (1)
	Desorbed	BCC	100	3.186 (1)
$(TiVNb)_{80}(CrAl)_{20}$	As-cast	BCC	100	3.162 (1)
	intermediate	BCT	72	3.073 (1) / 4.268 (1)
		BCC	28	3.293 (1)
	Desorbed	BCC	100	3.163 (1)
$(TiVNb)_{70}(CrAl)_{30}$	As-cast	BCC	100	3.147 (1)
	monohydride	BCC	100	3.236 (1)
	Desorbed	BCC	100	3.145 (1)
$(TiVNb)_{60}(CrAl)_{40}$	As-cast	BCC	100	3.128 (1)
	solid solution	BCC	100	3.171 (1)
	Desorbed	BCC	100	3.124 (1)

3.4. Experimental PCT diagrams and thermodynamic properties

Fig. 6 shows the PCT curves collected at 25°C for all $(TiVNb)_{100-x}(CrAl)_x$ alloys including the pristine ternary one. A two-step sequence of hydrogenation can be distinguished for the alloys with $x \leq 20$: the first plateau at low equilibrium pressure up to around 0.6-0.8 H/M is related to the formation of an intermediated BCC monohydride and the second plateau at higher pressure corresponds to the formation of the FCC or BCT dihydride phase with maximum capacity 1.5-2.0 H/M. The pressure value of the first plateau is within the limits of detection of the pressure transducer and were not plotted in Fig. 6. However, the presence of these two hydrogenation sequences became more obvious to be observed in the PCT curves recorded at different temperatures, as will be discussed below in Figs. 7a and 7c. This two-step

transition is typical for the hydrogenation process of both conventional BCC alloys and MPEAs [7,11,13,20]. For the alloys with x = 30 and 40 at.% only the first step could be recorded hinting that higher pressure is required to reach the equilibrium pressure of the second plateau to form full dihydride of these alloys. This finding is in good agreement with the capacity decrease observed in the kinetic measurements with increasing Cr/Al concentration.

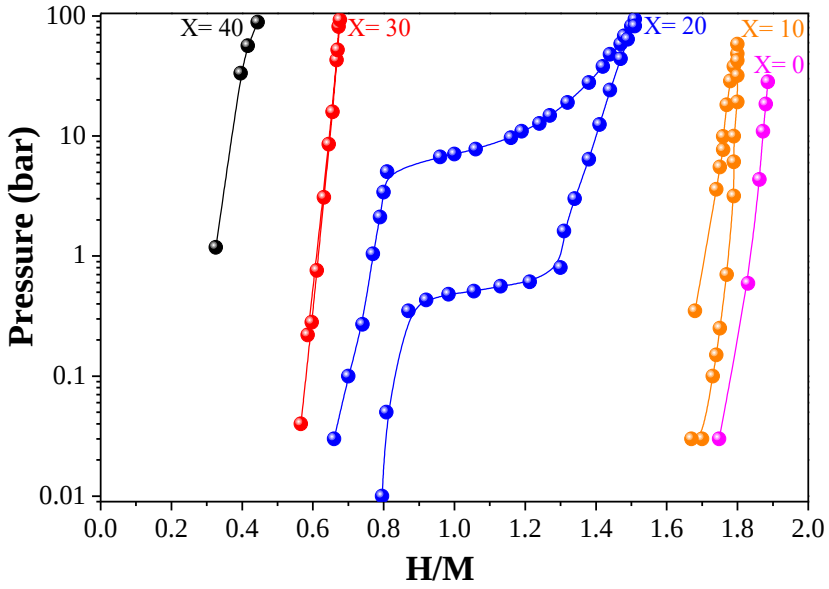

Fig. 6. Pressure-composition-temperature for the $(TiVNb)_{100-x}(CrAl)_x$ alloys recorded at 25 °C for the first absorption cycle. The PCT diagram of the ternary TiVNb alloy, already published elsewhere [20], has been included.

It is obvious that the maximum capacity depends on both the chemical composition and the maximum reachable pressure in the instrument. Increasing the Cr/Al content decreases the capacity and affects the absorption and desorption plateau pressures. The latter values increase with the raise of Cr/Al content and consequently, the maximum capacity cannot be longer achieved for x = 30 and 40 at.% under these experimental conditions.

Note that the desorption plateau pressure for the alloy with x = 20 at.% is 0.6 bar (close to standard pressure condition of 1 bar), which was not possible to achieve through only individual Cr [13,14] and Al [20,21] additions. Furthermore, it confirms that spontaneous desorption has occurred after the sample has been removed from the hydrogenation apparatus, which is in good agreement with the presence of both BCT and BCC hydrides identified after kinetic measurements at RT (see the XRD for the alloy with x = 20 in Fig. 5a). These results suggest that adequate control of Cr and Al contents in the TiVNb alloy may lead to a hydride that could have practical reversibility at room temperature. It is worth mentioning that the PCT curve of the $(TiVNb)_{80}(CrAl)_{20}$ alloy exhibits a pronounced hysteresis phenomenon, characterized by a significant difference of one order of magnitude between the absorption and desorption plateau pressures. This observation is consistent with previous reports on TiVNb-(Cr) alloys [13,14,26,29,30]. The hysteresis observed in metal hydrides, has been linked to various factors such as strain, particle size, defects concentration/generation, and plastic deformation [31]. However, despite significant research efforts, reducing or eliminating the hysteresis phenomenon in metal hydrides remains an unresolved topic in the literature. Finding effective strategies to mitigate hysteresis continues to be an active area of investigation.

Fig. 7 displays the PCT curves recorded at different temperatures and the related Van't Hoff plots for the alloys with x = 10 and x = 20. The enthalpies and entropies for hydrogen absorption and desorption for both alloys are listed in Table 3. For comparison, the available thermodynamic properties of the TiVNb, TiVNb-(Cr) and TiVNb-(Al) systems were also included. It is worth mentioning that, for each temperature, a fresh sample was used for these measurements. The effect of equimolar Cr/Al addition on the absorption reaction of $(TiVNb)_{100-x}(CrAl)_x$ alloys gradually decreases the enthalpy values from -67 to -49 and -34 kJ/mol H_2 for x = 0 [20], 10 and 20, respectively. Interestingly, the experimental enthalpy for hydrogen

absorption for the $(TiVNb)_{90}(CrAl)_{10}$ alloy was similar to the observed values for the $(TiVNb)_{70}Cr_{30}$ and $(TiVNb)_{90}Al_{10}$ alloys, see Table 3.

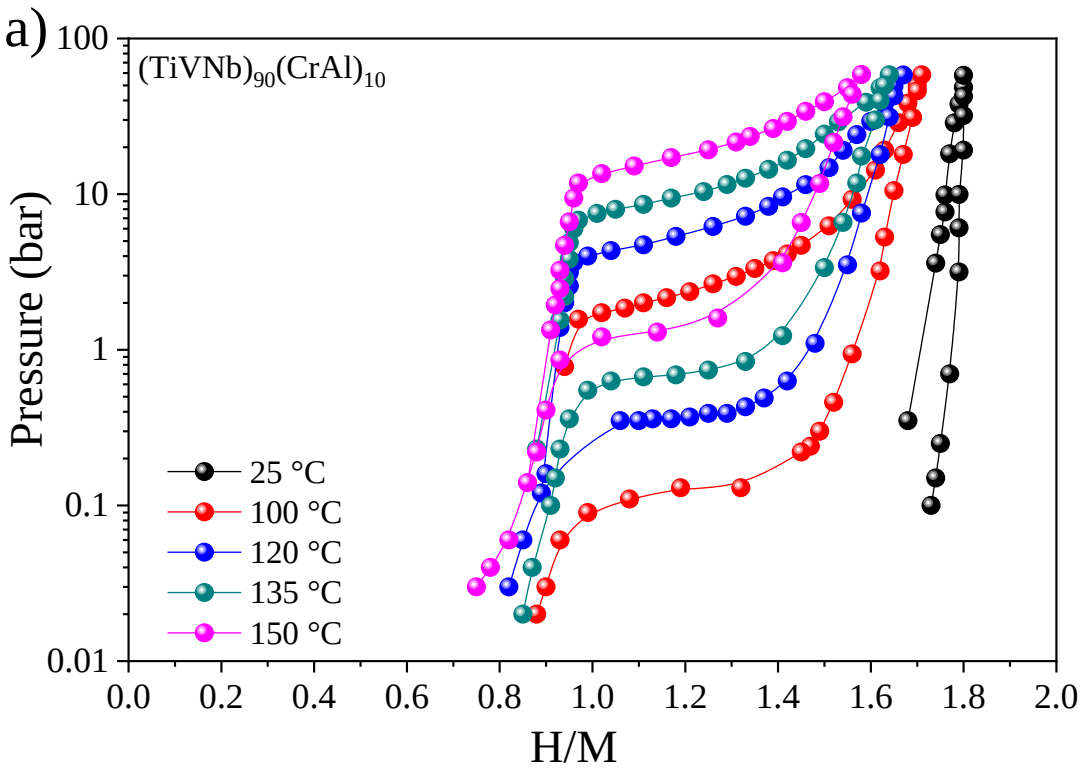

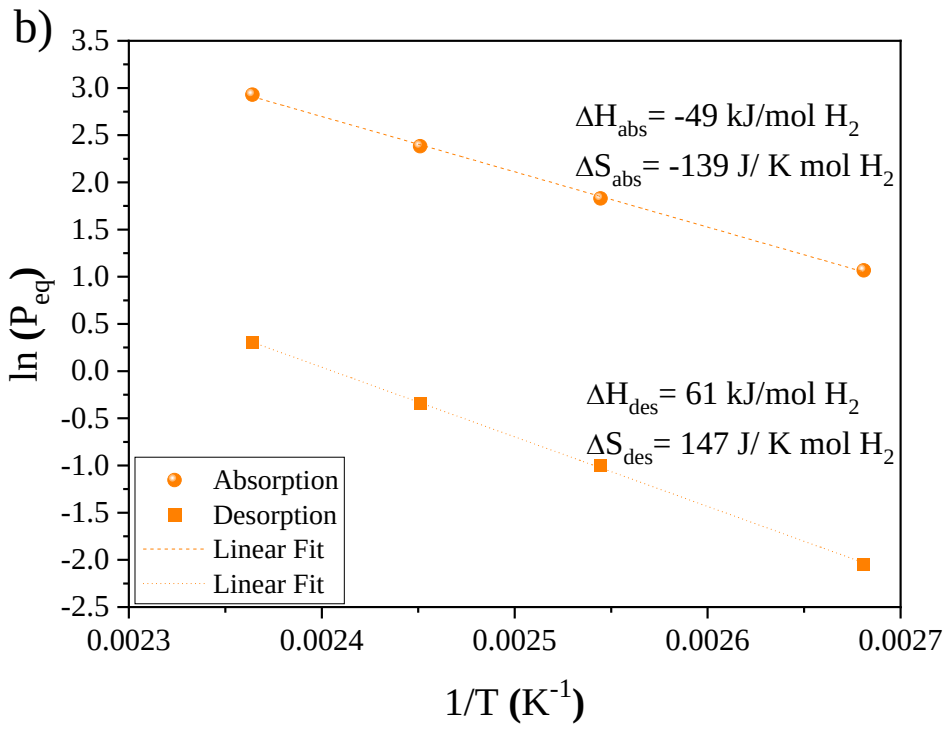

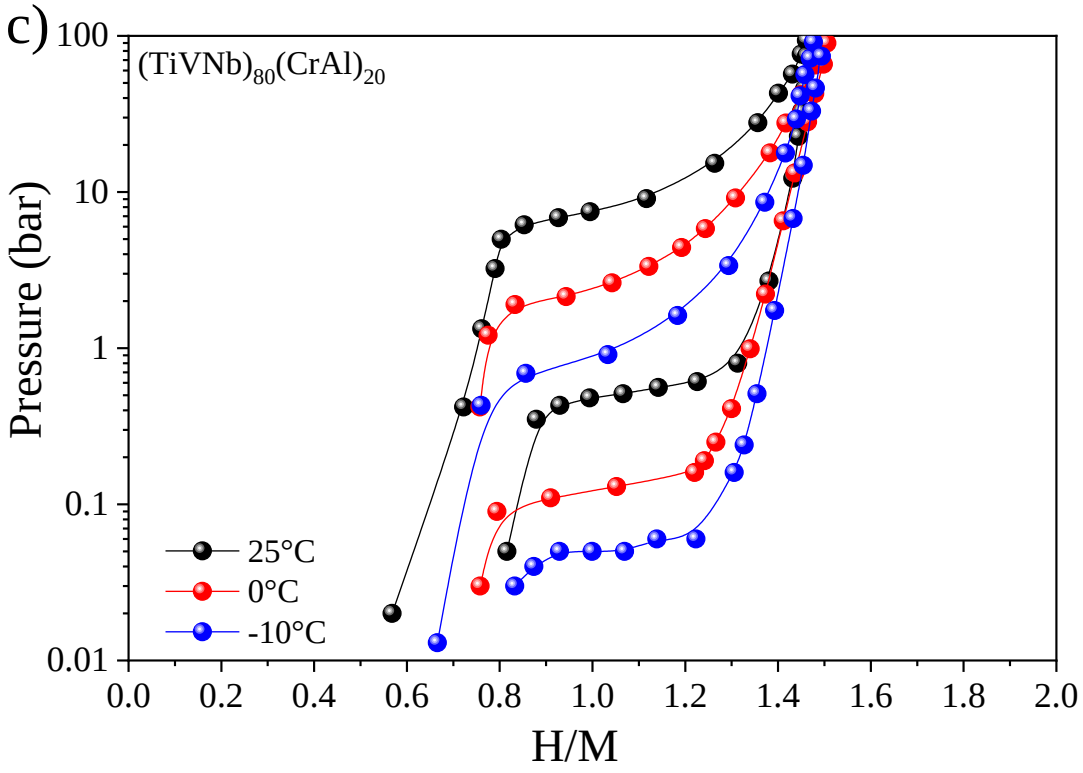

1

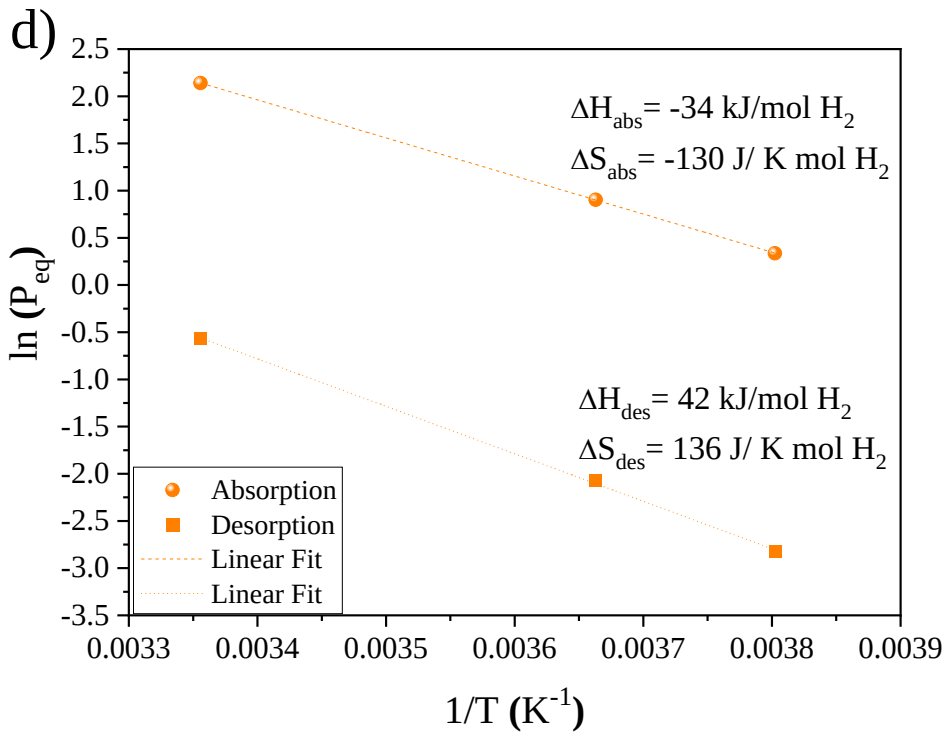

2

3 **Fig. 7.** PCT curves and corresponding van't Hoff plot for absorption and desorption of hydrogen

4 for the: (a-b) $(TiVNb)_{90}(CrAl)_{10}$ and (c-d) $(TiVNb)_{80}(CrAl)_{20}$ alloys, respectively.

Table 3 – Thermodynamic properties for hydrogen absorption and desorption reaction of the $(TiVNb)_{90}(CrAl)_{10}$ and $(TiVNb)_{80}(CrAl)_{20}$ alloys. Available thermodynamic properties of the TiVNb, TiVNb-(Cr) and TiVNb-(Al) systems are included for comparison.

System	Alloy	ΔH_{Abs} (kJ/mol H_2)	ΔS_{Abs} (J/K.mol H_2)	ΔH_{Des} (kJ/mol H_2)	ΔS_{Des} (J/K.mol H_2)	Ref.
TiVNb	TiVNb	-67	-157	-	-	[20]
TiVNb-(Cr)	$(TiVNb)_{75}Cr_{25}$	-52	-129	49	107	[32]
	$(TiVNb)_{70}Cr_{30}$	-49	-154	54	155	[14]
	$(TiVNb)_{65}Cr_{35}$	-39	-134	44	137	[14]
TiVNb-(Al)	$(TiVNb)_{95}Al_5$	-52	-141	-	-	[21]
	$(TiVNb)_{90}Al_{10}$	-49	-154	-	-	[21]
TiVNb-(CrAl)	$(TiVNb)_{90}(CrAl)_{10}$	-49 (1)	-139 (2)	61 (1)	147 (2)	This work
	$(TiVNb)_{80}(CrAl)_{20}$	-34 (1)	-130 (1)	42 (1)	136 (4)	This work

Comparing the experimental thermodynamic properties for the TiVNb-Al, TiVNb-Cr and TiVNb-(Cr/Al) systems (Table 3), one can see that the addition of both 10 at.% of Cr and 10 at.% of Al leads to the strongest thermodynamic destabilization as compared to the addition of 35 at.% Cr into the TiVNb alloy. These results suggest that Al has a greater influence on the thermodynamic properties than Cr. To illustrate this effect, we plotted the values of the enthalpy of hydrogen absorption in Table 3 as function of Al, Cr content in Figure 8. It is obvious that Al in TiVNb has a much stronger effect on the thermodynamics of TiVNb-(Cr/Al) than Cr. It is interesting to notice that this effect of Al addition in BCC-MPEAs has also been observed for V-Al BCC solid solutions [33,34]. In both materials, a decrease in enthalpy and stability of the final hydrides with an increase in Al content was observed.

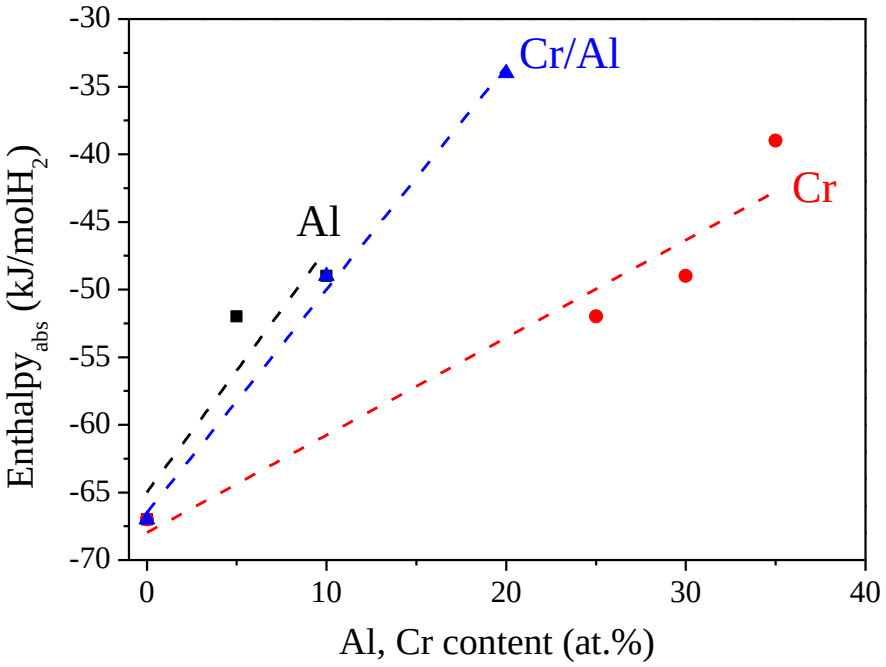

Fig. 8. Enthalpy for hydrogen absorption of the TiVNb alloy as a function of Al and/or Cr contents

Aiming to further understand the role of Cr and Al additions on the thermodynamic properties, the enthalpy of formation of the BCC solid solution was calculated by the CALPHAD method as a function of Cr and Al at 1273 K, Fig. 9. For this calculation performed at 1273 K, the TiVNb is a BCC solid solution whereas, the Cr and Al pure elements were considered BCC and FCC, respectively, in the reference state.

From Fig. 9, one can see that the addition of Cr (dashed line) in the TiVNb alloy leads to a more positive contribution in the heat of formation: it tends to destabilize the BCC solid solution up to 40 at.% Cr. This is in good agreement with the recent work published by Strozi et al. [14], which showed that a further increase of the Cr content from 35 at.% to 40 at.% stabilizes a mixture of C15 and BCC phases.

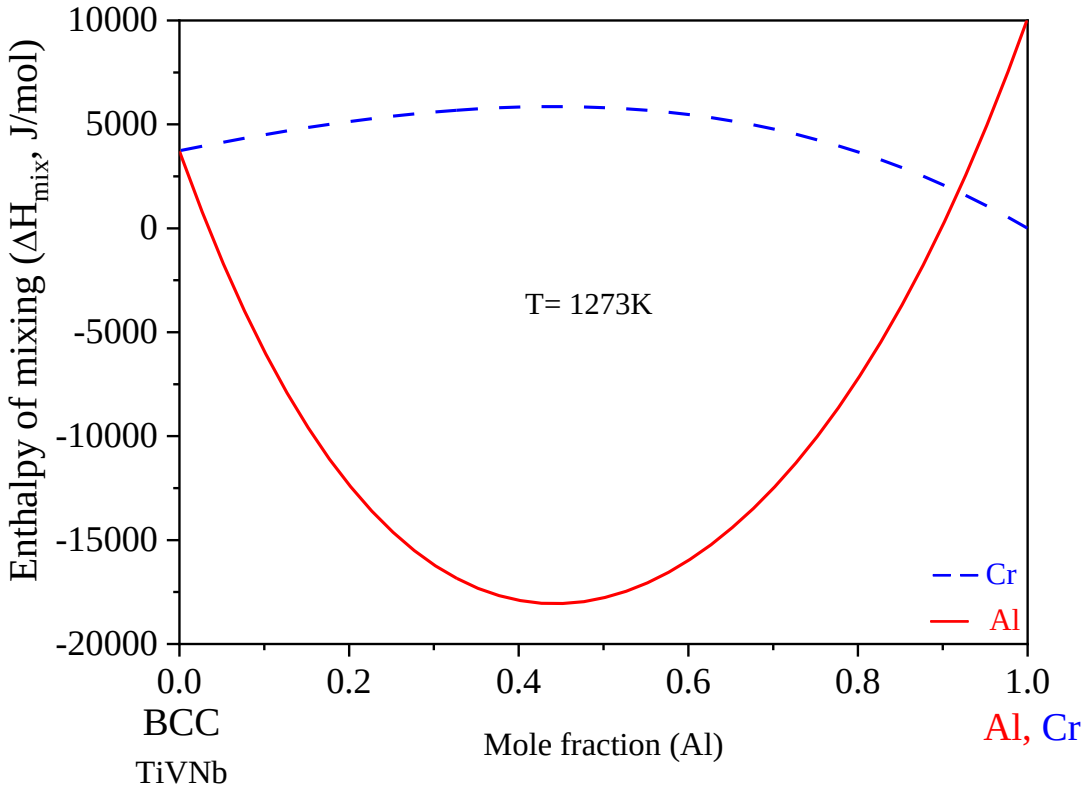

Fig. 9. Calculated enthalpy of mixing of the BCC solid solution from the pure elements in reference state considered at 1273 K (Cr, Nb, Ti and V = BCC; Al = FCC) as a function of: Cr (dashed line) and Al (solid line) contents at 1273 K.

In contrast, in Fig. 9, the addition of Al (solid line) into the TiVNb alloy results in a significant negative contribution in the heat of formation: the BCC solid solution tends to be more stable for compositions up to 50 at.% Al. This result agrees with several works that have attributed the addition of Al into MPEAs as a stabilizer of the BCC structure [17,35]. Furthermore, this finding can be linked with the reversed stability rule between the alloy and the related hydride proposed by Miedema and coworkers [36,37]. Miedema suggests that there is a competition between the stability of the alloy (or compound) and that of its hydride: the more stable the alloy, the less stable the related hydride and *vice versa*. Additionally, it is

noteworthy that AlH_3 hydrides [38] are less stable than CrH hydrides [39]. Thus, based on the results shown in Figure 9 and Miedema's rule one can expect that Al presence in TiVNb destabilizes more importantly the corresponding hydrides than Cr, which is in good agreement with experiments.

3.5. Hydrogen desorption

Hydrogen desorption properties of the hydrides were investigated using TDS by applying a heating rate of 5 °C/min and the TDS profiles are plotted in Fig. 10a. For the alloys with x = 0 and 10, this technique allows to probe the desorption properties of the FCC dihydride phases whereas for higher Cr/Al contents, we can only investigate the desorption from a mixture of hydrides (BCT + BCC for x = 20 at.%) or BCC solid solutions (for x = 30 and 40 at.%). One can notice that the onset temperature of hydrogen desorption for alloys with x = 10 and 20 at.% occurs at lower temperatures than the ternary TiVNb alloy. The $(TiVNb)_{80}(CrAl)_{20}$ alloy also showed a hydrogen desorption event in a shorter temperature range compared to the $(TiVNb)_{90}(CrAl)_{10}$ alloy. This can be associated with the lower absorption capacity (1.44 H/M) and with the spontaneous desorption of the unstable BCT hydride.

The variation in the T_{onset} for hydrogen desorption as a function of Cr/Al content into the $(TiVNb)_{100-x}(CrAl)_x$ alloys is shown in Fig 10b. A clear decreasing tendency of this parameter can be seen for the alloys that formed FCC and BCT dihydrides (x = 10 and 20, respectively) as compared to the pristine ternary alloy [20]. Based on the studies available in the literature on the individual Cr [14] and Al [20,21] additions into the TiVNb alloy, this effect can be mainly attributed to the presence of Al. Frequently, T_{onset} for hydrogen desorption has been linked to the valence electron concentration (VEC). These studies show that for some specific MPEA systems, a linear relationship between VEC and T_{onset} could be observed

[11,40]. An increase of the T_{onset} is proposed with the raise of VEC. A similar trend could be observed for the present alloys with x = 0 [20], 10 and 20, as depicted in Figure S9 from the Supplementary material. However, it is important to mention that this relationship between the VEC parameter and the hydrogen storage properties in MPEAs is an open discussion in the literature. For example, Silva et al. [26] investigated three MPEAs with the same VEC= 4.87 and showed that the T_{onset} was affected by the Cr, Co and Ni substitution into the TiVNb alloy system and not by a change in the VEC.

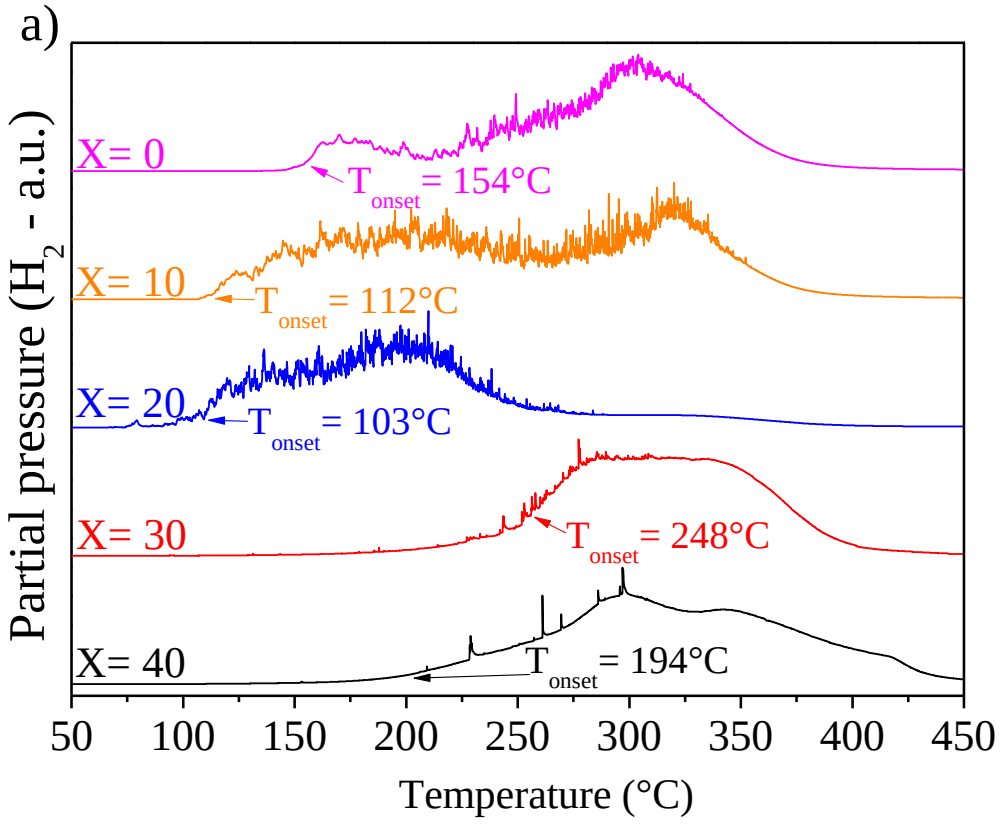

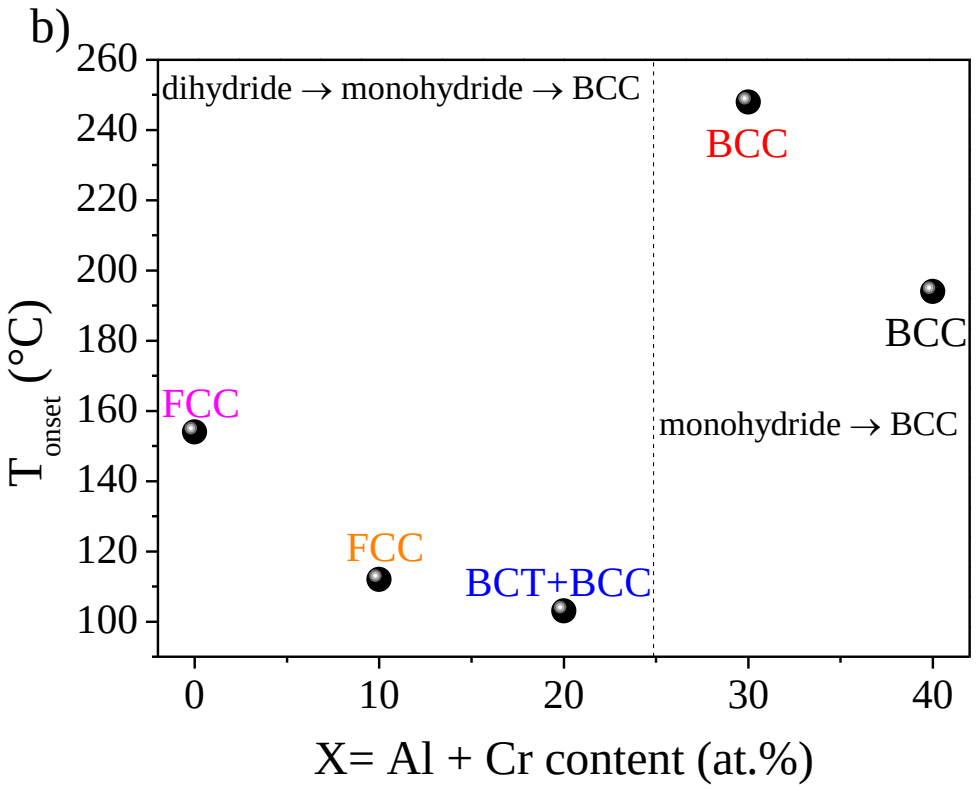

Fig. 10. (a) Thermo-desorption spectroscopy profiles of hydrides samples from the first cycle of hydrogenation for the $(TiVNb)_{100-x}(CrAl)_x$ alloys. A heating ramp of 5 °C/min was employed. (b) Variation in the onset temperature for hydrogen desorption as a function of Cr and Al content for the $(TiVNb)_{100-x}(CrAl)_x$ alloys. The TDS profile of the TiVNb alloy [20] has been included.

The XRD patterns of the desorbed samples after TDS experiments are displayed in Figure S10 of the supplementary data. From the corresponding Rietveld refinements (Figure S11 from the Supplementary Materials), all the desorbed materials recover the initial BCC structure with lattice parameter very similar to the initial alloys, see Table 2. These results indicate that the hydrogen absorption/desorption reactions for the $(TiVNb)_{100-x}(CrAl)_x$ alloys with x = 10, 20, 30 and 40 at.% are fully reversible.

3.6. Cyclability at room temperature

It is obvious from PCT experiments that the only alloy that can be cycled isothermally at 25 °C is the $(TiVNb)_{80}(CrAl)_{20}$ alloy between the BCT dihydride and the BCC monohydride phases. Thus, the hydrogen absorption/desorption reversibility at 25 °C was assessed over 20 cycles, as displayed in Fig. 11. The hydrogenation was carried out under 90 bar of hydrogen pressure the desorption procedure was performed by exposing the sample to dynamic secondary vacuum for 120 min at 25 °C.

For the first absorption reaction, the maximum capacity of 1.44 H/M (2.4 wt.%) was achieved, in agreement with the kinetics and PCT measurements. From subsequent cycles, the alloy reaches a stable reversible capacity of about 0.8 H/M (1.4 wt.%) which corresponds to reversible reaction between the dihydride and the monohydride phases. The observed drop in values from 1.4 H/M to 0.8 H/M after the first cycle is not indicative of a reduction in the hydrogen storage capacity of the $(TiVNb)_{80}(CrAl)_{20}$ alloy. Instead, it reflects the absorption/desorption reversibility between the BCT dihydride and BCC monohydride phases, which takes place spontaneously under ambient conditions. Remarkably, unlike other BCC-MPEAs systems where complete reversibility relies on temperature-assisted desorption, the $(TiVNb)_{80}(CrAl)_{20}$ alloy exhibits reversibility between the BCT dihydride and BCC monohydride phases without the need for additional external stimuli, highlighting its exceptional behavior.

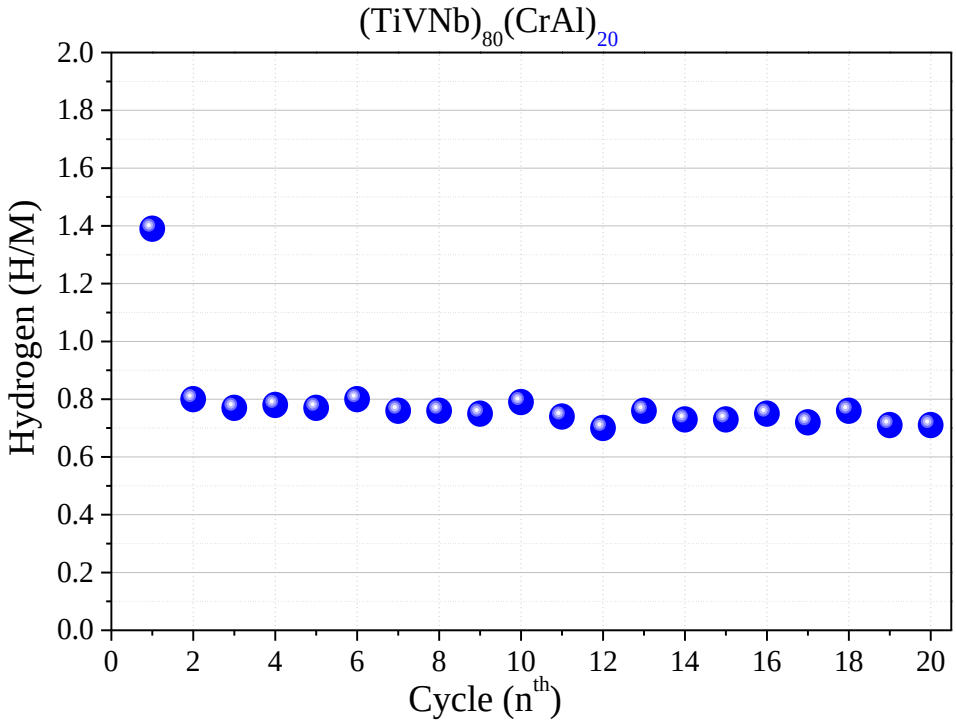

Fig. 11. Reversible hydrogen absorption capacity of the $(TiVNb)_{80}(CrAl)_{20}$ alloy at RT.

For further cycling, a slight decrease of the capacity from 0.8 H/M to 0.7 H/M on the 20^{th} cycle is noticed, which corresponds to a reduction of 12.5%. This slight reduction might be explained by the increase in the defect's concentration over the cycles, which might be accounted by the broadening of the XRD peaks after cycling, Figure S12 from the Supplementary Materials. This behavior is frequently reported for BCC MPEAs over cycling [14,20,21,26,41]. The Rietveld analysis of the fully hydrogenated sample after 20 cycles shows that the coexistence of BCT and BCC hydrides is maintained in the but an amorphous phase is also present. The presence of this amorphous phase might reasonably explain the decrease in the capacity during cycling.

If the lattice parameters of the BCT and BCC hydrides remained almost similar after the first absorption and the 20^{th} cycle, the phase fraction is different, and this may be reasonably accounted by the spontaneous hydrogen desorption from this material.

Therefore, the combined Cr and Al additions proves to be a promising strategy for hydride destabilization and to overcome the thermodynamic barrier found for individual Cr addition (35 at.% Cr), allowing a greater range of tuning of the hydrogen storage properties of BCC-MPEAs.

4. Conclusions

In this work, a strategy to decrease the stability of the dihydride phases formed in the TiVNb alloy from Cr/Al addition was presented through the study of the hydrogen absorption/desorption properties of $(TiVNb)_{100-x}(CrAl)_x$ alloys with x = 10, 20, 30, and 40 at.%. The PCT diagrams and the thermodynamic properties revealed that the combined addition of these two non-hydrides forming elements has a strong effect on the second plateau pressure resulting in a thermodynamic destabilization of the hydride formation. Specifically, the following conclusions were reached:

- The arc-melted alloys with x = 10, 20, 30, and 40 formed predominantly BCC solid solutions with decreasing lattice parameter by increasing the Cr/Al content.
- SEM observations reveal the formation of dendritic microstructures with the dendrites slightly richer in Nb.
- The alloys with x = 10 and 20 quickly absorb hydrogen at room temperature forming dihydrides whereas, the compositions with higher Cr/Al content don't form full hydrides under our experimental conditions.
- Chromium and aluminum decrease the stability of the related dihydrides. We demonstrated that Al has a greater effect on the thermodynamics than Cr, also supported by CALPHAD calculations.
- The onset temperature for hydrogen desorption from dihydride phases decreased when the Cr/Al content increases.

- Among all materials, the $(TiVNb)_{80}(CrAl)_{20}$ alloy possesses the optimal thermodynamic properties for isothermal cycling at room temperature between dihydride and monohydride phases. This composition reaches a reversible stable capacity of about 0.8 H/M (1.4 wt.%) during absorption/desorption cycling.

Acknowledgements

This work was financially supported in part by the CAPES-COFECUB cooperation program (process number 88887.660219/2021-00, project number 88887.191910/2018-00), in by the Serrapilheira Institute (grant number Serra-1709-17362), in part by the Brazilian National Council Scientific and Technological Development (CNPq grant number, 309467/2021-7). The authors would like to thank Fabrice Couturas, Valérie Lalanne, Anis Bouzidi as well as Rémy Pires from ICMPE for their help. Jean-Marc Joubert is acknowledged for his help with the CALPHAD calculations. This study was financed in part by the Coordenação de Aperfeiçoamento de Pessoal de Nível Superior - Brasil (CAPES) - Finance Code 001.

Data availability

The datasets generated in this work are available from the corresponding author on reasonable request.

Declaration of competing interests

The authors declare that they have no known competing financial interests or personal relationships that could have appeared to influence the work reported in this paper.

5. References

[1] G. Marbán, T. Valdés-Solís, Towards the hydrogen economy?, Int J Hydrogen Energy. 32 (2007) 1625–1637. https://doi.org/10.1016/j.ijhydene.2006.12.017.

[2] M. Hirscher, V.A. Yartys, M. Baricco, J. Bellosta von Colbe, D. Blanchard, R.C. Bowman, D.P. Broom, C.E. Buckley, F. Chang, P. Chen, Y.W. Cho, J.C. Crivello, F. Cuevas, W.I.F. David, P.E. de Jongh, R. v. Denys, M. Dornheim, M. Felderhoff, Y. Filinchuk, G.E. Froudakis, D.M. Grant, E.M.A. Gray, B.C. Hauback, T. He, T.D. Humphries, T.R. Jensen, S. Kim, Y. Kojima, M. Latroche, H.W. Li, M. v. Lototskyy, J.W. Makepeace, K.T. Møller, L. Naheed, P. Ngene, D. Noréus, M.M. Nygård, S. ichi Orimo, M. Paskevicius, L. Pasquini, D.B. Ravnsbæk, M. Veronica Sofianos, T.J. Udovic, T. Vegge, G.S. Walker, C.J. Webb, C. Weidenthaler, C. Zlotea, Materials for hydrogen-based energy storage – past, recent progress and future outlook, J Alloys Compd. 827 (2020). https://doi.org/10.1016/j.jallcom.2019.153548.

[3] L. George, S.K. Saxena, Structural stability of metal hydrides, alanates and borohydrides of alkali and alkali- earth elements: A review, Int J Hydrogen Energy. 35 (2010) 5454–5470. https://doi.org/10.1016/j.ijhydene.2010.03.078.

[4] N.A.A. Rusman, M. Dahari, A review on the current progress of metal hydrides material for solid-state hydrogen storage applications, Int J Hydrogen Energy. 41 (2016) 12108–12126. https://doi.org/10.1016/j.ijhydene.2016.05.244.

[5] J.W. Yeh, S.K. Chen, S.J. Lin, J.Y. Gan, T.S. Chin, T.T. Shun, C.H. Tsau, S.Y. Chang, Nanostructured high-entropy alloys with multiple principal elements: Novel alloy design concepts and outcomes, Adv Eng Mater. 6 (2004) 299–303. https://doi.org/10.1002/adem.200300567.

[6] D.B. Miracle, O.N. Senkov, A critical review of high entropy alloys and related concepts, Acta Mater. 122 (2017) 448–511. https://doi.org/10.1016/j.actamat.2016.08.081.

[7] M. Sahlberg, D. Karlsson, C. Zlotea, U. Jansson, Superior hydrogen storage in high entropy alloys, Sci Rep. 6 (2016). https://doi.org/10.1038/srep36770.

[8] F. Marques, M. Balcerzak, F. Winkelmann, G. Zepon, M. Felderhoff, Review and outlook on high-entropy alloys for hydrogen storage, Energy Environ Sci. 14 (2021) 5191–5227. https://doi.org/10.1039/d1ee01543e.

[9] M. Sahlberg, D. Karlsson, C. Zlotea, U. Jansson, Superior hydrogen storage in high entropy alloys, Sci Rep. 6 (2016). https://doi.org/10.1038/srep36770.

[10] C. Zlotea, M.A. Sow, G. Ek, J.P. Couzinié, L. Perrière, I. Guillot, J. Bourgon, K.T. Møller, T.R. Jensen, E. Akiba, M. Sahlberg, Hydrogen sorption in TiZrNbHfTa high entropy alloy, J Alloys Compd. 775 (2019) 667–674. https://doi.org/10.1016/j.jallcom.2018.10.108.

[11] M.M. Nygård, G. Ek, D. Karlsson, M.H. Sørby, M. Sahlberg, B.C. Hauback, Counting electrons - A new approach to tailor the hydrogen sorption properties of

high-entropy alloys, Acta Mater. 175 (2019) 121–129. https://doi.org/10.1016/j.actamat.2019.06.002.

[12] G. Zepon, B.H. Silva, C. Zlotea, W.J. Botta, Y. Champion, Thermodynamic modelling of hydrogen-multicomponent alloy systems: Calculating pressure-composition-temperature diagrams, Acta Mater. 215 (2021). https://doi.org/10.1016/j.actamat.2021.117070.

[13] R.B. Strozi, D.R. Leiva, G. Zepon, W.J. Botta, J. Huot, Effects of the chromium content in (Tivnb)100−xcrx body-centered cubic high entropy alloys designed for hydrogen storage applications, Energies (Basel). 14 (2021). https://doi.org/10.3390/en14113068.

[14] R.B. Strozi, B.H. Silva, D.R. Leiva, C. Zlotea, W.J. Botta, G. Zepon, Tuning the hydrogen storage properties of Ti-V-Nb-Cr alloys by controlling the Cr/(TiVNb) ratio, J Alloys Compd. 932 (2023) 167609. https://doi.org/10.1016/j.jallcom.2022.167609.

[15] J. Graetz, J.J. Reilly, V.A. Yartys, J.P. Maehlen, B.M. Bulychev, V.E. Antonov, B.P. Tarasov, I.E. Gabis, Aluminum hydride as a hydrogen and energy storage material: Past, present and future, J Alloys Compd. 509 (2011). https://doi.org/10.1016/j.jallcom.2010.11.115.

[16] O.N. Senkov, S. v. Senkova, C. Woodward, Effect of aluminum on the microstructure and properties of two refractory high-entropy alloys, Acta Mater. 68 (2014) 214–228. https://doi.org/10.1016/j.actamat.2014.01.029.

[17] S.Y. Chen, X. Yang, K.A. Dahmen, P.K. Liaw, Y. Zhang, Microstructures and crackling noise of AlxNbTiMoV high entropy alloys, Entropy. 16 (2014) 870–884. https://doi.org/10.3390/e16020870.

[18] N.D. Stepanov, D.G. Shaysultanov, G.A. Salishchev, M.A. Tikhonovsky, Structure and mechanical properties of a light-weight AlNbTiV high entropy alloy, Mater Lett. 142 (2015) 153–155. https://doi.org/10.1016/j.matlet.2014.11.162.

[19] J. Montero, G. Ek, L. Laversenne, V. Nassif, M. Sahlberg, C. Zlotea, How 10 at% al addition in the ti-v-zr-nb high-entropy alloy changes hydrogen sorption properties, Molecules. 26 (2021). https://doi.org/10.3390/molecules26092470.

[20] N. Pineda-Romero, M. Witman, V. Stavila, C. Zlotea, The effect of 10 at.% Al addition on the hydrogen storage properties of the Ti0.33V0.33Nb0.33 multi-principal element alloy, Intermetallics (Barking). 146 (2022) 107590. https://doi.org/10.1016/j.intermet.2022.107590.

[21] N. Pineda-Romero, C. Zlotea, Uncovering the Effect of Al Addition on the Hydrogen Storage Properties of the Ternary TiVNb Alloy, Materials. 15 (2022) 7974. https://doi.org/10.3390/ma15227974.

[22] J.O. Andersson, T. Helander, L. Höglund, P. Shi, B. Sundman, Thermo-Calc & DICTRA, computational tools for materials science, CALPHAD. 26 (2002) 273–312. https://doi.org/10.1016/S0364-5916(02)00037-8.

[23] B.H. Toby, R.B. von Dreele, GSAS-II: The genesis of a modern open-source all purpose crystallography software package, J Appl Crystallogr. 46 (2013) 544–549. https://doi.org/10.1107/S0021889813003531.

[24] J. Huot, Metal Hydrides, in: Handbook of Hydrogen Storage: New Materials for Future Energy Storage, Wiley-VCH, 2010: pp. 81–116. https://doi.org/10.1002/9783527629800.ch4.

[25] N. Yurchenko, E. Panina, M. Tikhonovsky, G. Salishchev, S. Zherebtsov, N. Stepanov, A new refractory Ti-Nb-Hf-Al high entropy alloy strengthened by orthorhombic phase particles, Int J Refract Metals Hard Mater. 92 (2020) 105322. https://doi.org/10.1016/j.ijrmhm.2020.105322.

[26] B.H. Silva, C. Zlotea, Y. Champion, W.J. Botta, G. Zepon, Design of TiVNb-(Cr, Ni or Co) multicomponent alloys with the same valence electron concentration for hydrogen storage, J Alloys Compd. 865 (2021). https://doi.org/10.1016/j.jallcom.2021.158767.

[27] D. Banerjee, The intermetallic Ti2AlNb, Prog Mater Sci. 42 (1997) 135–158. https://doi.org/10.1016/s0079-6425(97)00012-1.

[28] Y.Q. Liu, W.T. Xu, D. Xie, Z.M. Li, Phase diagram calculations of Al-Cr-Nb-Ti quaternary system, Materials Research Innovations. 18 (2014) S2573–S2578. https://doi.org/10.1179/1432891714Z.000000000489.

[29] B. Hessel Silva, W.J. Botta, G. Zepon, Design of a Ti–V–Nb–Cr alloy with room temperature hydrogen absorption/desorption reversibility, Int J Hydrogen Energy. (2023). https://doi.org/10.1016/j.ijhydene.2023.05.032.

[30] B.H. Silva, C. Zlotea, G. Vaughan, Y. Champion, W.J. Botta, G. Zepon, Hydrogen absorption/desorption reactions of the (TiVNb)85Cr15 multicomponent alloy, J Alloys Compd. 901 (2022). https://doi.org/10.1016/j.jallcom.2022.163620.

[31] T.B. Flanagan, J.D. Clewley, Hysteresis in metal hydrides, Journal of The Less-Common Metals. 83 (1982) 127–141. https://doi.org/10.1016/0022-5088(82)90176-X.

[32] M.M. Nygård, Ø.S. Fjellvåg, M.H. Sørby, K. Sakaki, K. Ikeda, J. Armstrong, P. Vajeeston, W.A. Sławiński, H. Kim, A. Machida, Y. Nakamura, B.C. Hauback, The average and local structure of TiVCrNbDx (x=0,2.2,8) from total scattering and neutron spectroscopy, Acta Mater. 205 (2021). https://doi.org/10.1016/j.actamat.2020.116496.

[33] S. Kumar, M. Taxak, N. Krishnamurthy, A.K. Suri, G.P. Tiwari, Terminal solid solubility of hydrogen in V-Al solid solution, Int J Refract Metals Hard Mater. 31 (2012) 76–81. https://doi.org/10.1016/j.ijrmhm.2011.09.009.

[34] S. Kumar, S. Sonak, N. Krishnamurthy, Hydrogen solid solution thermodynamics of V1−xAlx (x: 0, 0.18, 0.37, 0.52) alloys, Int J Hydrogen Energy. 38 (2013) 9928–9934. https://doi.org/10.1016/j.ijhydene.2013.05.122.

[35] O.N. Senkov, S. v. Senkova, C. Woodward, Effect of aluminum on the microstructure and properties of two refractory high-entropy alloys, Acta Mater. 68 (2014) 214–228. https://doi.org/10.1016/j.actamat.2014.01.029.

[36] K.H.J. Buschow, C.P. Bouten, A.R. Miedema, Hydrides formed from intermetallic compounds of two transition metals: a special class of ternary alloys, 1982. http://iopscience.iop.org/0034-4885/45/9/001.

[37] A. Andreasen, R. (DK). M.R.Department. Risø National Lab., Predicting formation enthalpies of metal hydrides., 2004.

[38] B.C. Hauback, Structures of aluminium-based light weight hydrides, Zeitschrift Fur Kristallographie. 223 (2008) 636–648. https://doi.org/10.1524/zkri.2008.1020.

[39] M. Dottor, J.C. Crivello, J.M. Joubert, Thermodynamic modeling of Cr and Cr–H systems up to high temperatures and high pressures, Int J Hydrogen Energy. 47 (2022) 23293–23309. https://doi.org/10.1016/j.ijhydene.2022.04.245.

[40] C. Zlotea, A. Bouzidi, J. Montero, G. Ek, M. Sahlberg, Compositional effects on the hydrogen storage properties in a series of refractory high entropy alloys, Front Energy Res. 10 (2022). https://doi.org/10.3389/fenrg.2022.991447.

[41] J. Montero, G. Ek, L. Laversenne, V. Nassif, M. Sahlberg, C. Zlotea, How 10 at% al addition in the ti-v-zr-nb high-entropy alloy changes hydrogen sorption properties, Molecules. 26 (2021). https://doi.org/10.3390/molecules26092470.

Supplementary data

Tuning the hydride stability of the TiVNb-based alloys by equimolar Cr/Al addition

Tales Ferreira[a,b]*, Nayely Pineda-Romero[a], Walter José Botta[b], Guilherme Zepon[b], Claudia Zlotea[a]

[a] University Paris Est Créteil, CNRS, ICMPE, UMR 7182, 2 Rue Henri Dunant, 94320 Thiais, France

[b] Departamento de Engenharia de Materiais, Universidade Federal de São Carlos, São Carlos, Rod. Washington Luiz, km 235, São Carlos, SP 13565-905, Brazil

* Corresponding author. Postal address: University Paris Est Créteil, CNRS, ICMPE, UMR 7182, 2 Rue Henri Dunant, 94320 Thiais, France.

E-mail adresses: tferreira.tales@gmail.com (T. Ferreira).

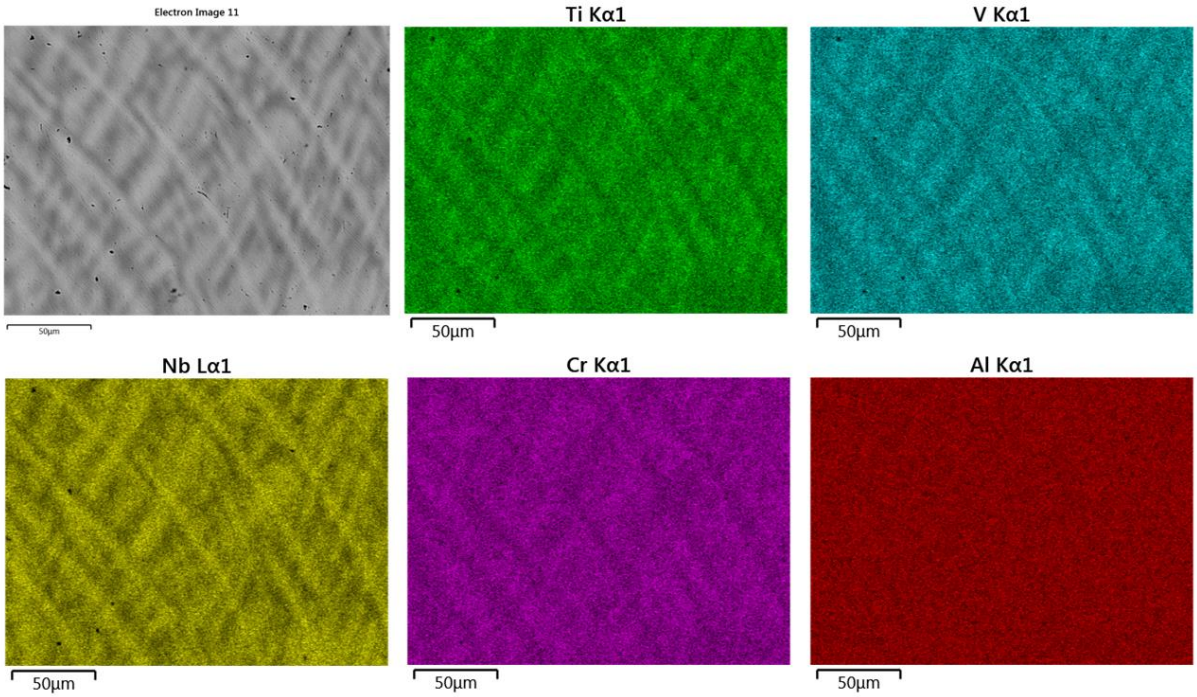

Figure S1 – Backscattered electron image and EDX-SEM chemical mapping analysis of the as-cast $(TiVNb)_{90}(CrAl)_{10}$ alloy.

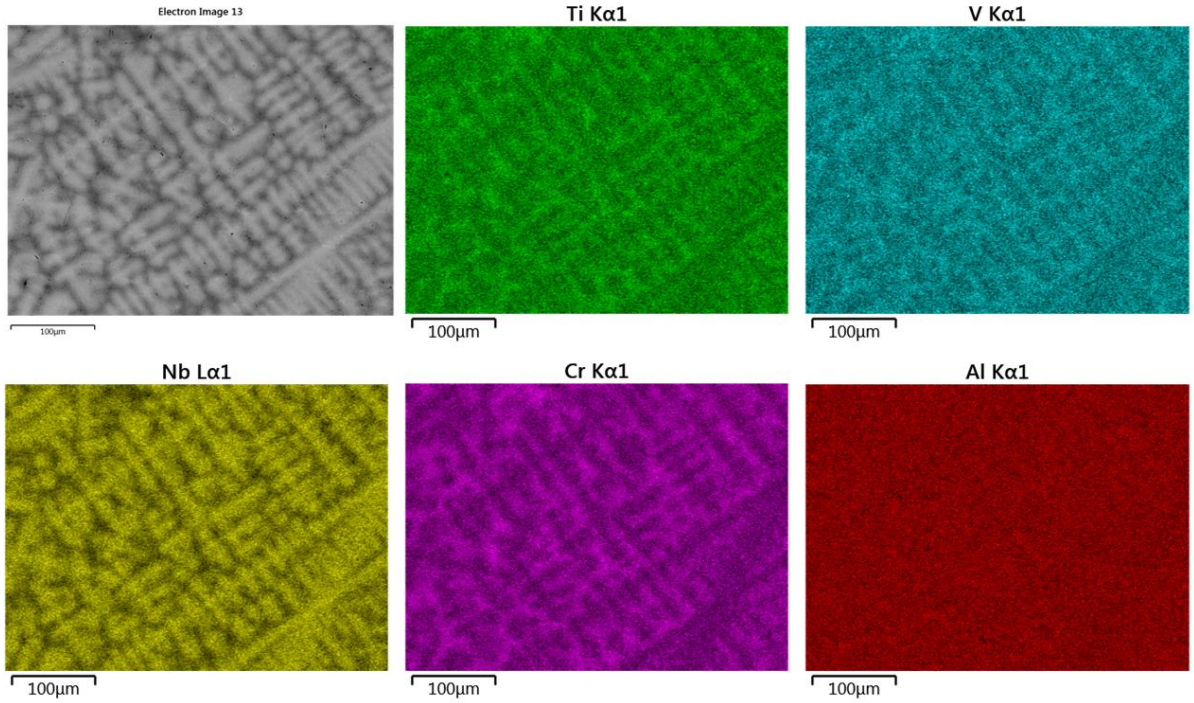

Figure S2 – Backscattered electron image and EDX-SEM chemical mapping analysis of the as-cast $(TiVNb)_{80}(CrAl)_{20}$ alloy.

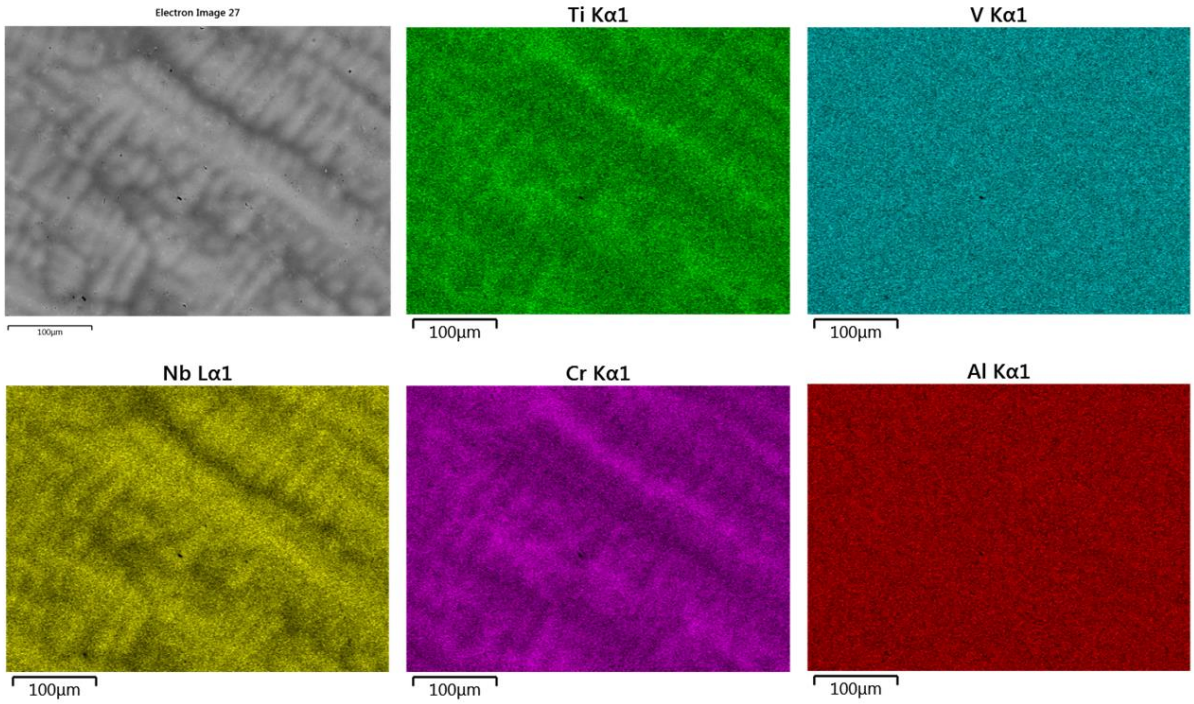

Figure S3 – Backscattered electron image and EDX-SEM chemical mapping analysis of the as-cast $(TiVNb)_{70}(CrAl)_{30}$ alloy.

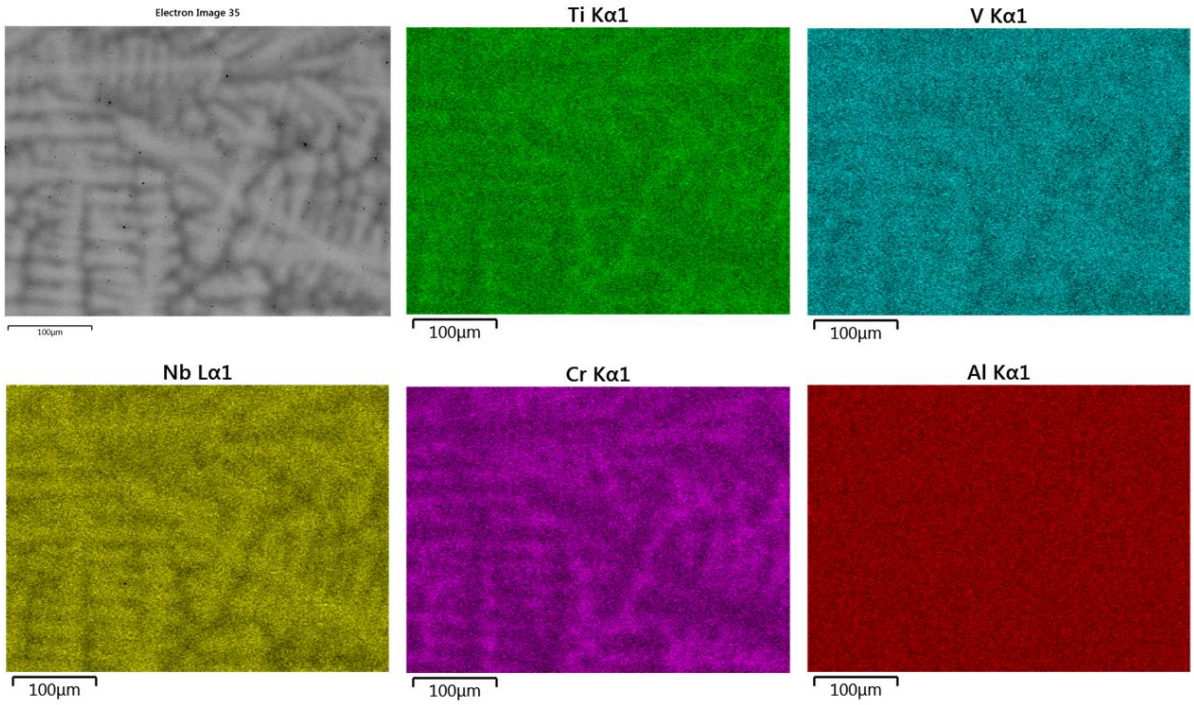

Figure S4 – Backscattered electron image and EDX-SEM chemical mapping analysis of the as-cast $(TiVNb)_{60}(CrAl)_{40}$ alloy.

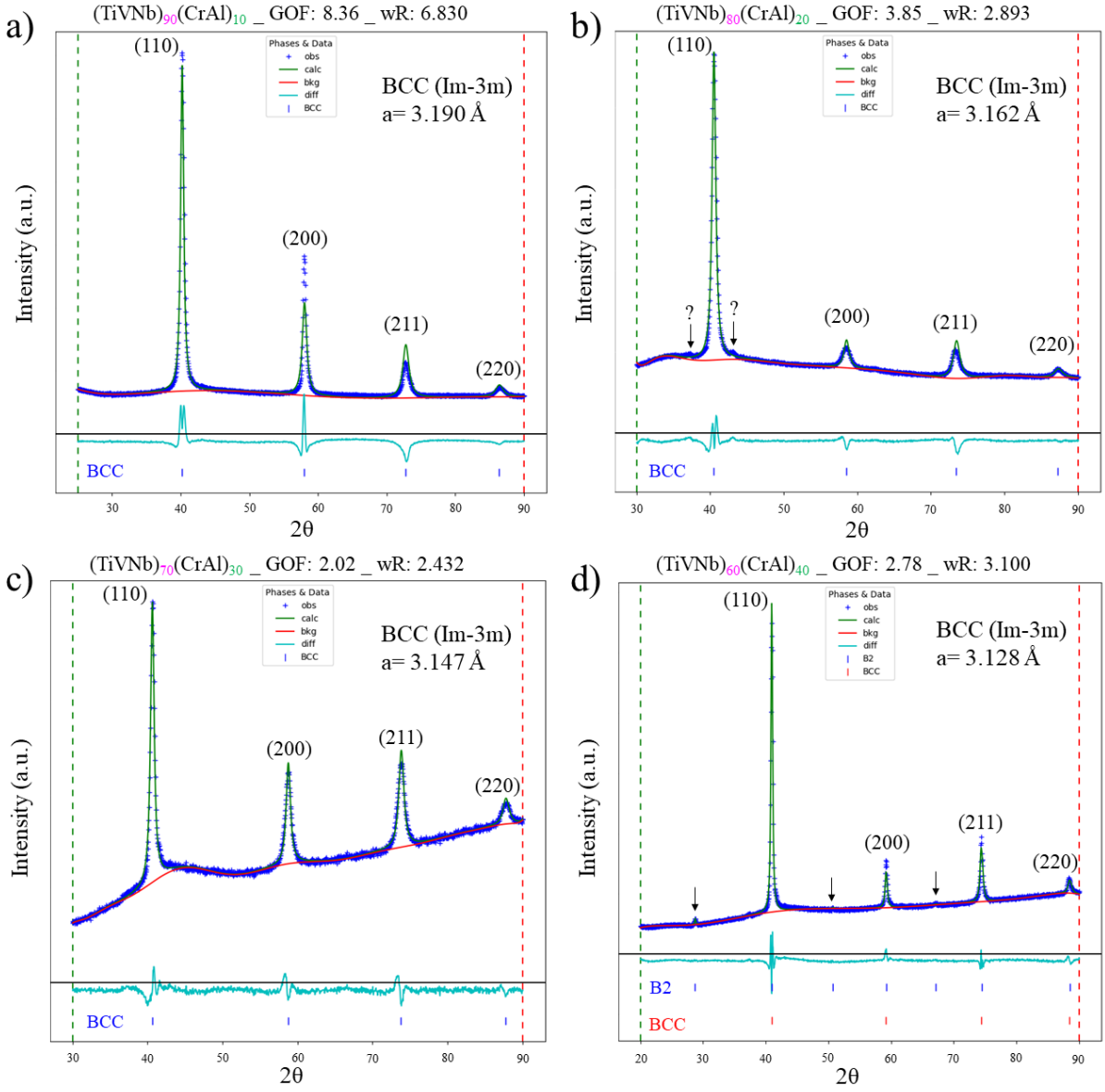

Figure S5 – Rietveld refinement analysis of the X-Ray diffraction (XRD) patterns for the $(TiVNb)_{100-X}(CrAl)_X$ series alloys, in the as-cast condition, with X= 10 (a), 20 (b), 30 (c), and 40 (d) at.%. The arrows indicate the presence of low intensity peaks in the XRD patterns of the alloys, suggesting a small fraction of secondary phases.

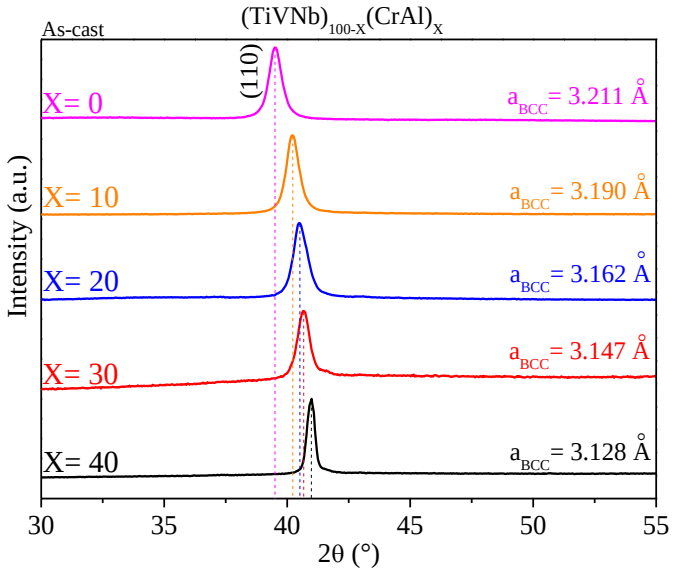

Figure S6 – Evolution of the main (100) peak position and BCC lattice parameter with equimolar Cr and Al additions into $(TiVNb)_{100-x}(CrAl)_x$ alloys.

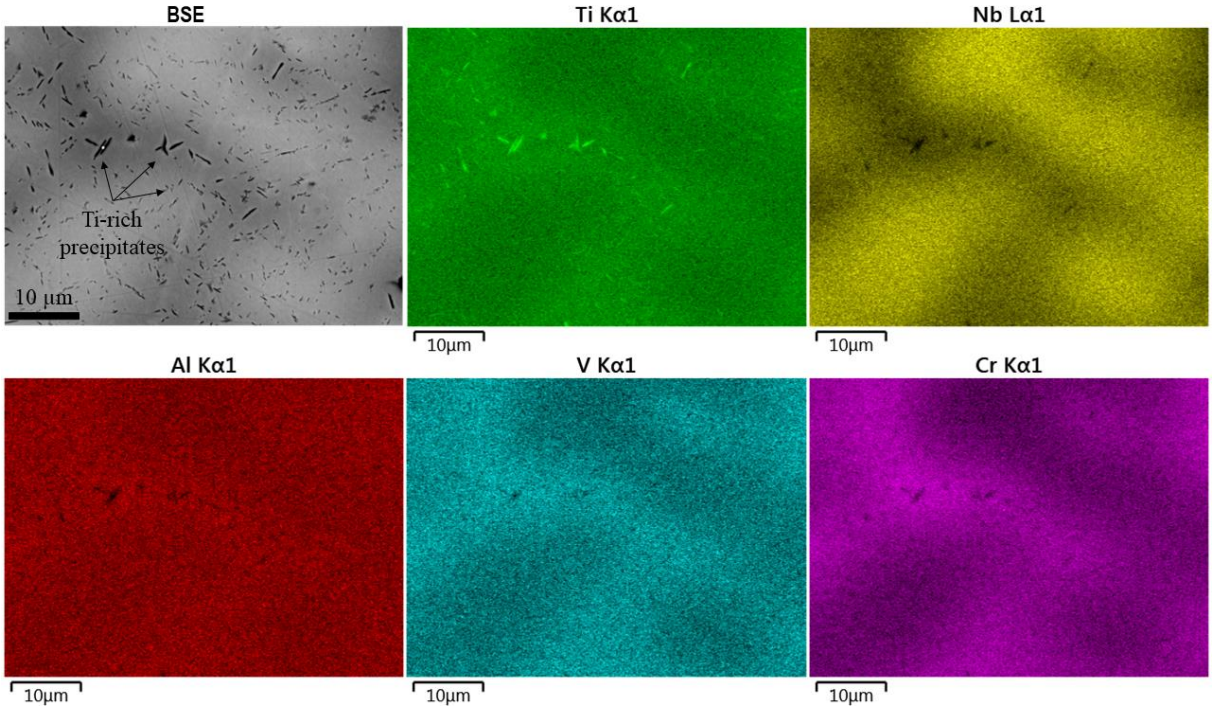

Figure S7 – Backscattered electron image and EDX-SEM chemical mapping analysis of the Ti-rich precipitates observed in the interdendritic regions of the $(TiVNb)_{80}(CrAl)_{20}$ alloy.

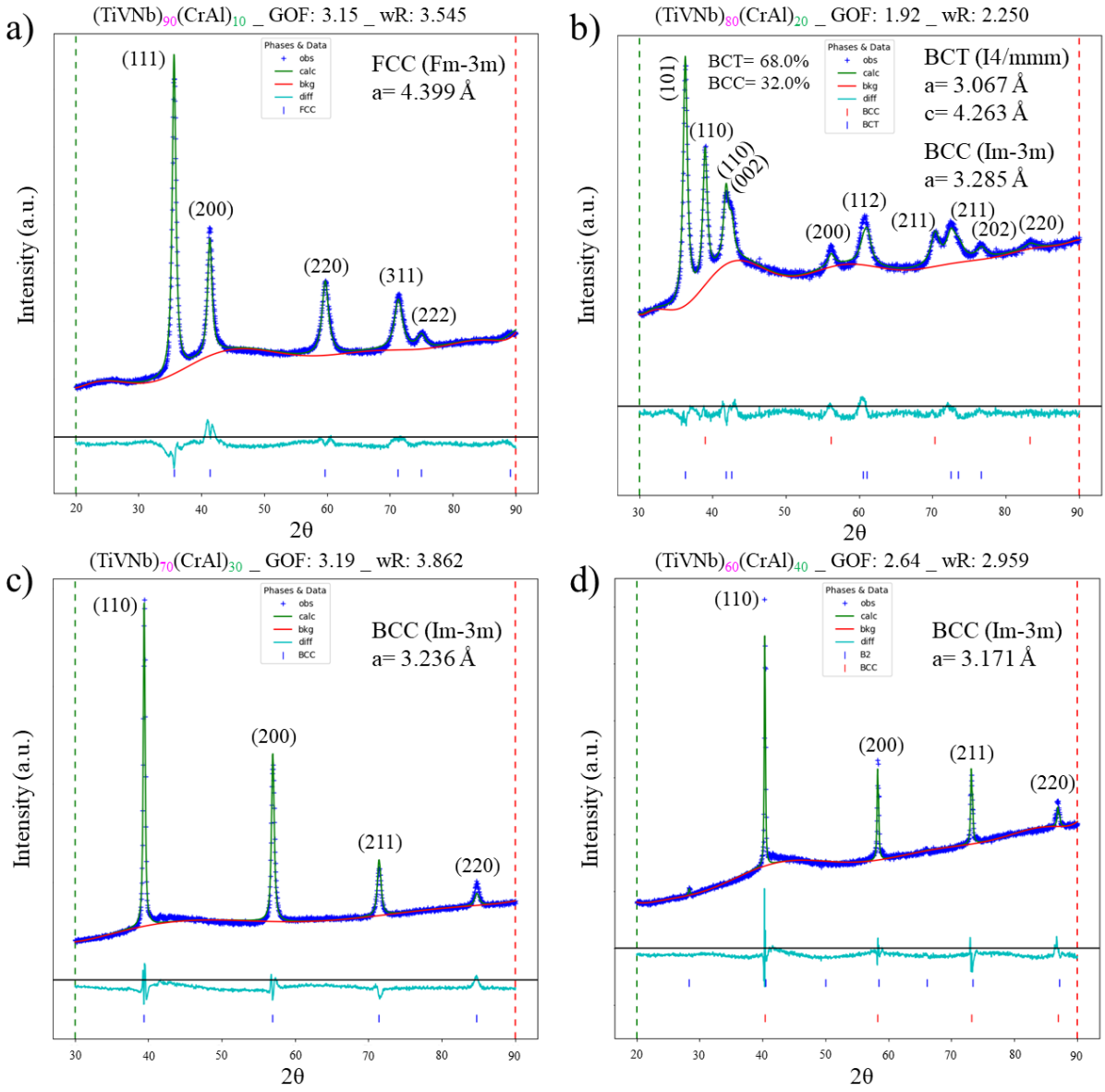

Figure S8 – Rietveld refinement analysis of the X-Ray diffraction (XRD) patterns for the fully hydrogenated $(TiVNb)_{100-x}(CrAl)_x$ alloys with x = 10 (a), 20 (b), 30 (c), and 40 (d) at.%.

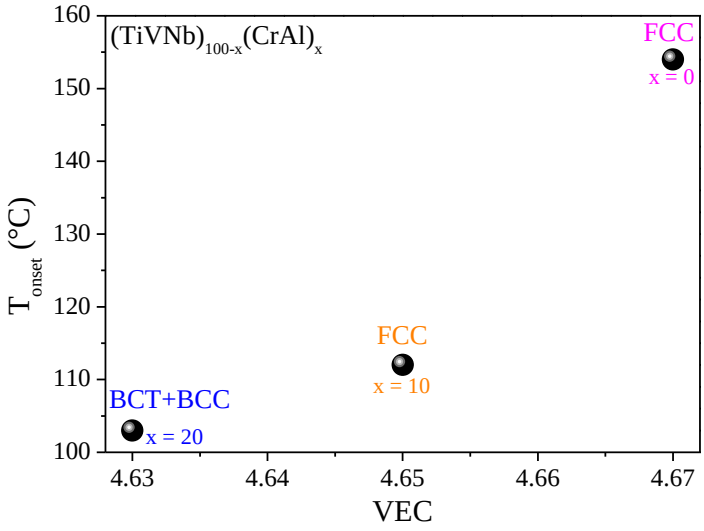

Figure S9 – The variation of the T_{onset} of desorption with VEC for the $(TiVNb)_{100-x}(CrAl)_x$ alloys with x = 0 [20], 10 and 20 at.%.

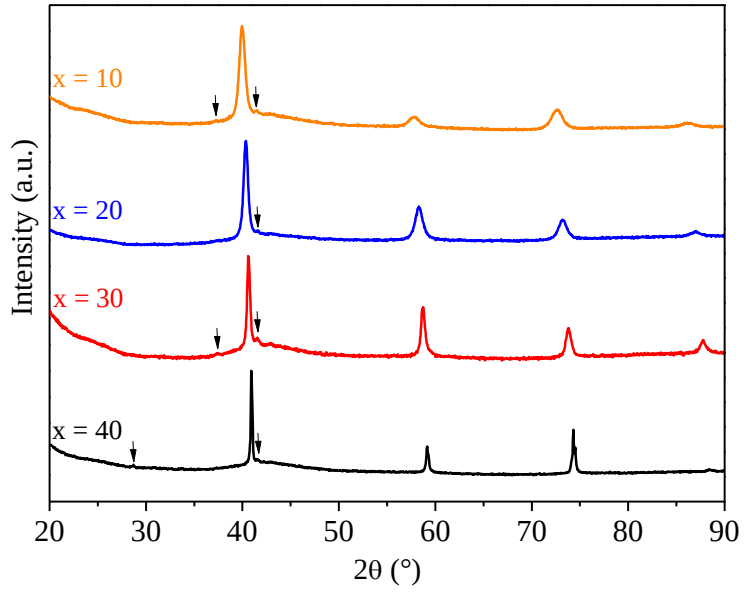

Figure S10 – XRD patterns of the $(TiVNb)_{100-x}(CrAl)_x$ alloys with x = 10, 20, 30 and 40 at.% after TDS. The arrows indicate the presence of low intensity peaks in the XRD patterns of the alloys, suggesting a small fraction of secondary phases.

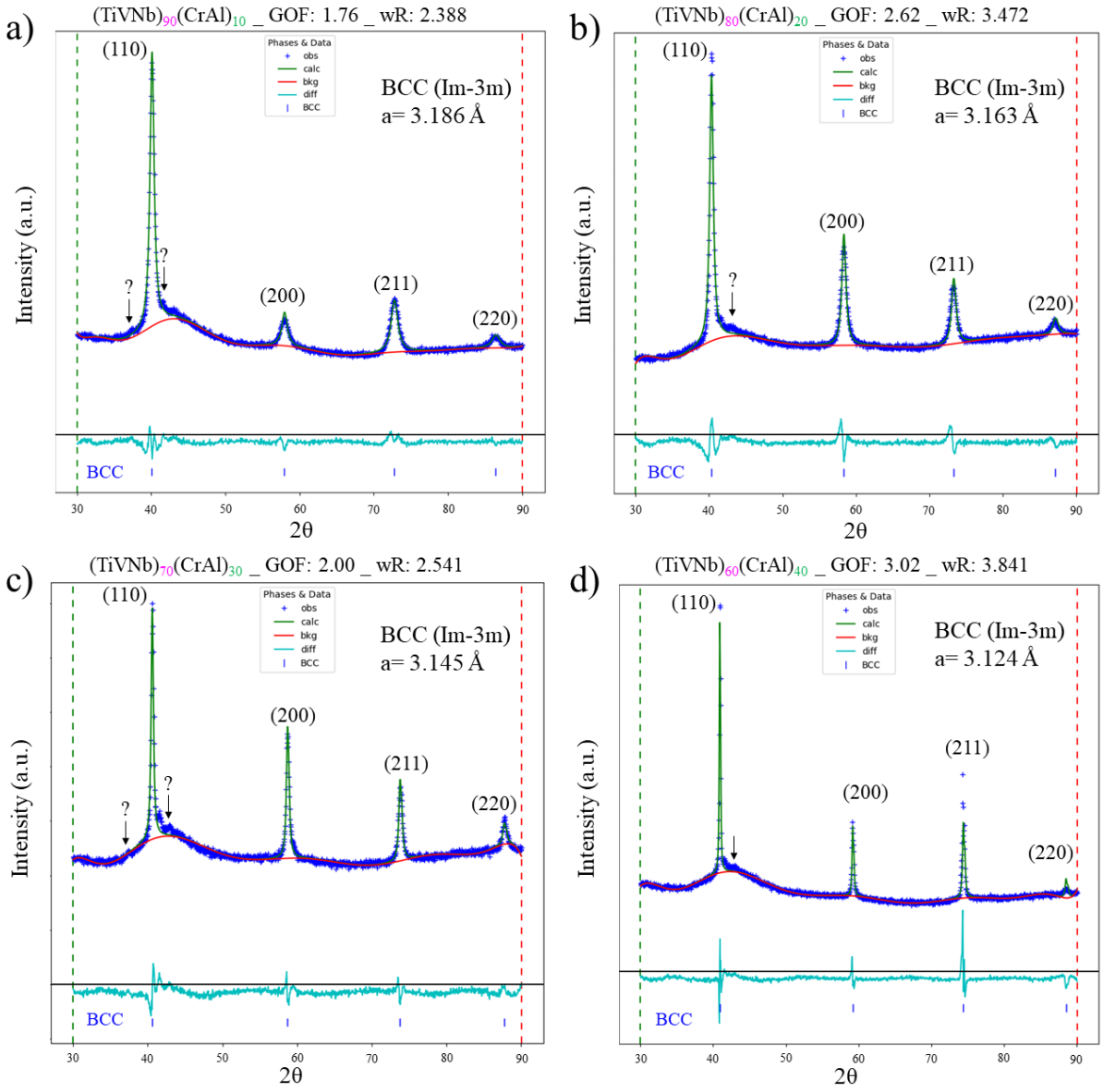

Figure S11 – Rietveld refinement analysis of the X-Ray diffraction (XRD) patterns after TDS for the $(TiVNb)_{100-X}(CrAl)_X$ alloys with X= 10 (a), 20 (b), 30 (c), and 40 (d) at.%. The arrows indicate the presence of low intensity peaks in the XRD patterns of the alloys, suggesting a small fraction of secondary phases. The amorphous region in the XRD patterns is related to the presence of amorphous SiO2 fibers that were used as a filter during TDS measurements.

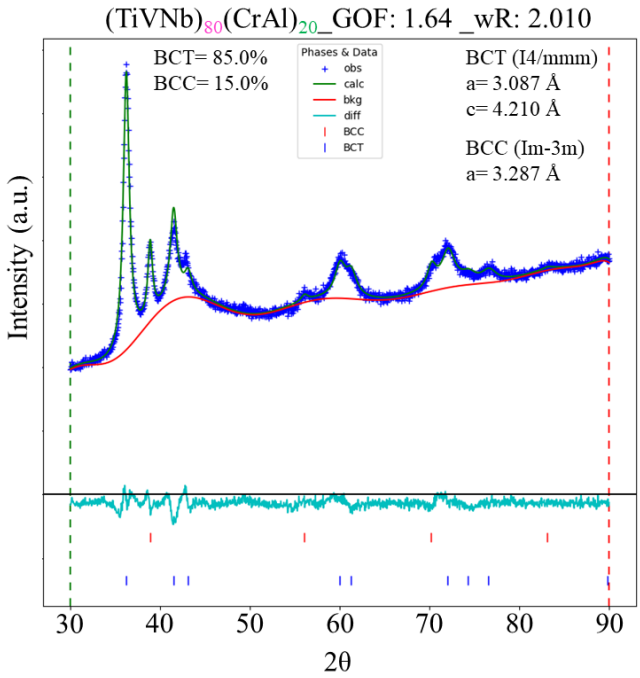

Figure S12 – Rietveld refinement analysis of the X-Ray diffraction (XRD) pattern for the fully hydrogenated $(TiVNb)_{80}(CrAl)_{20}$ alloy after 20 cycles at room temperature.